Available online at www.sciencedirect.com
SCIENCE DIRECT®
Icarus 170 (2004) 70–90
ICARUS
www.elsevier.com/locate/icarus

Photometric modeling of Saturn's rings. II. Azimuthal asymmetry in reflected and transmitted light

H. Salo,[a,*] R. Karjalainen,[a] and R.G. French [b]

[a] *Department of Physical Sciences, Astronomy Division, PO BOX 3000, FI-90014 University of Oulu, Finland*
[b] *Astronomy Department, Wellesley College, Wellesley, MA 02481, USA*

Received 12 September 2003; revised 10 March 2004

Available online 18 May 2004

Abstract

Dynamical *N*-body simulations (Salo, 1992, Nature 359, 619) suggest the formation of trailing density enhancements in the outer portions of Saturn's rings, due to local gravitational instabilities. These Julian–Toomre type wakes, having a pitch angle of about 20°–25° with respect to the local tangential direction, seem to provide a plausible explanation for the observed quadrupole brightness variation in Saturn's A ring (Salo and Karjalainen, 1999, Bull. Am. Astron. Soc. 31, 1160; French et al., 2000, Bull. Am. Astron. Soc. 32, 806; Porco et al., 2001, Bull. Am. Astron. Soc. 33, 1091). We have carried out systematic photometric modeling of gravitational wake structures seen in dynamical simulations, performed for the parameter values of the A ring, using the Monte Carlo radiative transfer code described in Salo and Karjalainen (2003, Icarus 164, 428). Comparisons to the observed asymmetry in various cases are presented (asymmetry in reflected and transmitted light, ring longitude and opening angle dependence), in all cases confirming the applicability of the wake model. Typically, minimum brightness corresponds to viewing/illumination along the long axis of wakes; however, the sense of modeled asymmetry reverses at small tilt angles in diffuse transmission. Implications of wakes on the occultation optical depth profiles and the A ring overall brightness behavior are also discussed: it is shown that the wake structure needs to be taken into account when the Cassini occultation profiles for the A ring are interpreted in terms of variations in surface density. Also, the presence of wakes offers a plausible explanation for the inverse tilt effect seen in the mid A-ring.

Keywords: Planetary rings; Saturn; Radiative transfer; Collisional physics; Computer techniques

1. Introduction

The outer parts of Saturn's rings exhibit bisymmetric azimuthal brightness variations, first noticed by Camichel (1958), and later confirmed by Ferrin (1975) and Reitsema et al. (1976). According to these observations the brightness of the A ring has two minima, before the western and eastern ansae, in the sense of rotation of the rings. Subsequent detailed studies (Lumme and Irvine, 1976a, 1979b; Lumme et al., 1977; Thompson et al., 1981) confirmed the 180° symmetry of the brightness variations and showed that a similar asymmetry is seen in all visual wavelengths, and that the amplitude of the asymmetry peaks when the ring opening angle is around 12°. In these ground-based observations the minimum brightness is seen at longitudes of about 245°–250° and 65°–70°, measured with respect to the sub-observer point in the direction of the orbital motion. However, due to the small range of phase angles accessible from Earth, it is difficult to distinguish whether the minimum is predominantly related to the observing or illumination direction. The detailed analysis of low-phase Voyager images (Dones et al., 1993) showed that the amplitude of variations peaks strongly in the mid-A ring, reaching a full amplitude $((I_{\max} - I_{\min})/\langle I \rangle)$ of about 35% in reflected light at the saturnocentric distance of 128,000 km. Also, the longitude of the minimum seemed to be mainly determined by the viewing direction. The A ring asymmetry is also seen in transmitted light (Franklin et al., 1987), whereas for the B ring no asymmetry was detected. Note that Saturn's rings have often been reported to show a difference between the visual brightnesses of the East and West ansae, the ampli-

* Corresponding author. Fax: +358-8-553-1934.
E-mail address: heikki.salo@oulu.fi (H. Salo).

0019-1035/$ – see front matter
doi:10.1016/j.icarus.2004.03.012

tude and sign of which varies with time ("east–west asymmetry," see, e.g., Piironen and Lukkari (1980) and detailed references therein). This phenomenon, if real, is likely to be distinct from the permanently present quadrupole asymmetry addressed here: it has been suggested to rise due to reflection by debris clouds caused by meteoroidal impacts on the rings (Hämeen-Anttila and Itävuo, 1976).

A likely cause of the azimuthal quadrupole brightness asymmetry is small-scale particle inhomogeneities, trailing by about 20°–25° with respect to the local tangential direction (Colombo et al., 1976). As discussed in Franklin et al. (1987), such systematically oriented inhomogeneities could arise due to dynamical wakes excited around massive particle aggregates (Franklin and Colombo, 1978; Karttunen, 1983), or from the superposition of numerous Julian–Toomre (1966) gravity wakes excited about the ring particles themselves (see Franklin et al., 1987; Dones and Porco, 1989). In both cases the expected orientation of the wakes is determined by the differential rotation, which for a Keplerian velocity field yields $\phi_{\rm wake} \sim 20°$. Other models in terms of elongated swarms of particle debris resulting from collisions have also been discussed (Gorkavyi and Taidakova, 1989, see Fridman and Gorkavyi, 1999, p. 122), but these require additional assumptions about the lifetime of the debris swarms, in order to yield the desired orientation. The large maximum amplitude of the asymmetry suggests that, whatever structures are responsible for the brightness variations, they need to cover a large fraction of the ring area, at least in the mid-A ring, and have a very large intrinsic brightness contrast. This seems to favor Julian–Toomre type spontaneous wakes over those forced by embedded moonlets, unless the latter are much more abundant than usually assumed. Moreover, the formation of trailing Julian–Toomre wakes via local gravitational instabilities has been confirmed by numerical N-body simulations (Salo, 1992), with parameter values consistent with Voyager measurements of size distribution and surface density, using the Bridges et al. (1984) laboratory measurements of the elasticity of icy particles.

The ability of density wakes to cause brightness variations follows from the fact that the fractional reflecting surface area will be direction-dependent (see Fig. 1). In particular, when the wakes are viewed more or less along their long axis, the rarefied regions between the dense wakes are better visible, reducing the overall reflection, in comparison to the perpendicular viewing direction when the rarefied regions are partially hidden (see, e.g., Franklin et al., 1987; Thompson, 1982; Dones and Porco, 1989). The direction of illumination is likewise expected to have importance, as well as the multiple scattering occurring predominantly inside wakes. Somewhat different models, in terms of multiple scattering in optically thick ellipsoidal particle blobs (Lumme and Irvine, 1979a) yield the same expected dependence of longitude minima and maxima with respect to the assumed orientation of the blobs. A-ring wakes also manifest themselves in the asymmetry of Saturn's microwave thermal

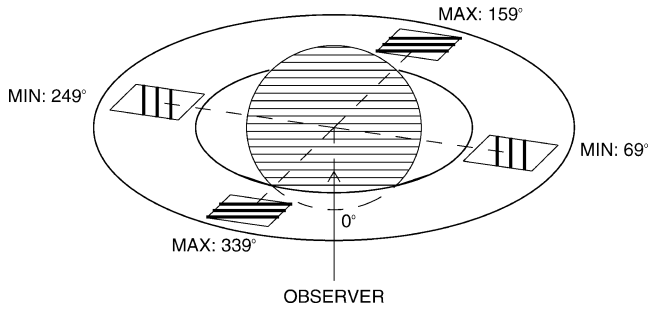

Fig. 1. Schematic explanation for the relation of wake structure to azimuthal asymmetry. At low elevation angles the wakes trailing by about 21° with respect to the local tangential direction are seen roughly along their long axis at ring longitudes of 249° and 69°, and perpendicular to their long axis at longitudes of 339° and 159°. In the former case rarefied regions between wakes are visible, reducing the reflecting surface area: this should correspond to minimum brightness. In the latter case rarefied regions are hidden by the wakes in low tilt angle images, maximizing the reflecting area and thus corresponding to maximum brightness. For a more realistic illustration, see Fig. 3.

radiation transmitted through the rings (Dunn et al., 2004). Wake structure has also been suggested to explain the asymmetry in the thermal radiation scattered by the rings (van der Tak et al., 1999; Dunn et al., 2002); due to Saturn being the source of radiation this asymmetry manifests as a difference between East and West ansae (not to be confused with the visual 'east–west asymmetry' mentioned above).

We have carried out photometric modeling of Julian–Toomre wake structures seen in dynamical simulations, and have made systematic comparisons to the observed asymmetry at various geometries. The photometric calculation method, based on Monte Carlo modeling of light rays scattered by a system of discrete simulation particles, as well as its application to azimuthally homogeneous ring models, has been described in Salo and Karjalainen (2003) (hereafter Paper I). Some preliminary results for the asymmetry have already been reported in Salo and Karjalainen (1999), Salo et al. (2000), and French et al. (2000), supporting the wake explanation for the asymmetry (see also Porco et al., 2001). In the present study we demonstrate that wakes obtained via dynamical simulations can account naturally for several basic properties of the asymmetry, including the tilt-angle dependence found in ground-based observations, as well as the longitude dependence in Voyager observations of both reflected and transmitted light. Implications for the occultation optical depth are also briefly discussed, as well as the consequences of wakes on the elevation angle dependence (tilt effect) of the A ring brightness. Two different dynamical simulation runs are studied, for the distances corresponding to the maximum of the observed asymmetry amplitude, using models (1) with identical particles and (2) with a truncated power-law size distribution, for a fixed value of surface density, corresponding to that typically assumed for the mid-A ring. Here, we are primarily interested in exploring the differences between these two models, rather than trying to achieve an exact match with observations. The next paper in

this series will study the dependence of the simulated asymmetry on various dynamical parameters: the saturnocentric distance, the internal density and elasticity of particles, the ring surface density, and the size distribution of particles.

2. Gravitational wakes and the asymmetry

2.1. Gravitational instability in planetary rings

The local equilibrium state in planetary rings is governed by the balance between collisional dissipation and the viscous gain of energy from the systematic velocity field. In the absence of self-gravity the resulting equilibrium velocity dispersion is determined by the elastic properties of particles and by their size distribution. Due to mutual gravity, particles tend to form density enhancements via local gravitational instability. This tendency for gravitational collapse is opposed by the velocity dispersion of particles and by differential rotation, which stabilize disturbances on small and large scales, respectively (Toomre, 1964). The condition for axisymmetric gravitational stability is that the Toomre parameter $Q > 1$, where

$$Q = \frac{\sigma_r \kappa}{3.36 G \Sigma} \tag{1}$$

measures the velocity dispersion. Here σ_r and Σ represent the radial velocity dispersion and the surface density, respectively, and the epicyclic frequency κ equals the angular frequency Ω in the case of a Keplerian velocity field. In practice, even if Q exceeds unity but remains below 2–3, significant non-axisymmetric local condensations may form (Julian and Toomre, 1966; Salo, 1992, 1995; Daisaka and Ida, 1999). Due to differential rotation, these condensations appear in the form of trailing wakes, inclined typically by $\sim 20^\circ$ with respect to the tangential direction. These forming condensations heat the system, so that in the absence of dissipative collisions the ring would soon become featureless again as Q rises to $\gg 1$. In the presence of impacts a statistical steady-state is reached, with new wakes replacing the old ones which disperse in timescales of order of the orbital period. The typical radial scale of wakes in simulations corresponds, at least roughly, to Toomre's critical wavelength (Toomre, 1964),

$$\lambda_{\rm cr} = 4\pi^2 G \Sigma / \kappa^2, \tag{2}$$

which for the parameter values of Saturn's rings corresponds to

$$\lambda_{\rm cr} = 70\ {\rm m} \left(\frac{a}{10^8\ {\rm m}} \right)^3 \left(\frac{\Sigma}{1000\ {\rm kg\,m^{-2}}} \right). \tag{3}$$

The rough requirement for the formation of wakes, $Q < 2$, indicates for identical particles with radius r and internal density ρ (in which case $\Sigma = \frac{4}{3}\rho r \tau$) that

$$\frac{\sigma_r}{r\Omega} < 14 \left(\frac{a}{10^8\ {\rm m}} \right)^3 \left(\frac{\rho}{900\ {\rm kg\,m^{-3}}} \right) \tau. \tag{4}$$

Since the minimum velocity dispersion maintained by impacts alone may be estimated to be about $2–3 r\Omega$ (in the case of identical particles and a constant coefficient of restitution, see Brahic, 1977; Wisdom and Tremaine, 1988; Salo, 1995), it is clear that rarefied ring regions with $\tau < \tau_{\rm min}$ are stable against the formation of wakes: the above minimum velocity dispersion $2–3 r\Omega$, combined with Eq. (4) indicates

$$\tau_{\rm min} \approx 0.2 \left(\frac{a}{10^8\ {\rm m}} \right)^{-3} \left(\frac{\rho}{900\ {\rm kg\,m^{-3}}} \right)^{-1}, \tag{5}$$

or about 0.3–0.1, from the inner C ring to the outer A ring, if the density of solid ice is assumed. In regions with $\tau > \tau_{\rm min}$ wakes *may* form, depending on the actual elasticity law, the internal density of particles, and the particles' size distribution. Namely, in the presence of a size distribution, small particles achieve a larger velocity dispersion than the larger ones, which acts as a stabilizing factor. The importance of the elasticity law stems from the fact that in the case of a velocity dependent coefficient of restitution $\epsilon_n = \epsilon(v)$, the system can attain, depending on the exact form of the velocity dependence, a steady-state with a finite velocity dispersion $\sigma_r \gg r\Omega$, in contrast to the case of constant ϵ_n, leading to σ_r a few times $r\Omega$ whenever the system is thermally stable: $\epsilon_n < \epsilon_{\rm cr}$, where $\epsilon_{\rm cr} \approx 0.65$ for $\tau \to 0$ (Hämeen-Anttila, 1978; Goldreich and Tremaine, 1978). The internal density is also important, since for a small ρ the maximum space density is limited even in the case of close packing of particles. Taking into account these uncertainties, dynamical N-body simulations seem to offer the most reliable way to address the formation and properties of the gravity wakes in Saturn's rings.

2.2. Dynamical simulations

In the present study we want to address the general applicability of gravity wakes to explain the observed azimuthal asymmetry, as well to illustrate some other possible photometric consequences of wake structure. For this purpose just a few typical simulation examples are studied, with dynamical parameters chosen to represent the mid A ring where the asymmetry is most pronounced. The simulations are performed with a local method described in Salo (1995). The basic idea in the method is to restrict all collisional and gravitational calculations to a small region inside the rings, co-moving with the local mean angular speed of particles. Linearized dynamical equations are employed, and the particles leaving the simulation system due to differential rotation are treated by using periodic boundary conditions, first introduced in Wisdom and Tremaine (1988) and Toomre and Kalnajs (1991). As discussed in Paper I, these periodic boundary conditions are straightforward to incorporate into photometric calculations.

An example of the time evolution in a dynamical simulation is shown in Fig. 2, for internal density $\rho = 450\ {\rm kg\,m^{-3}}$, dynamical optical depth $\tau_{\rm dyn} = 0.5$ and saturnocentric distance $a = 130{,}000$ km. Identical particles are used, with the

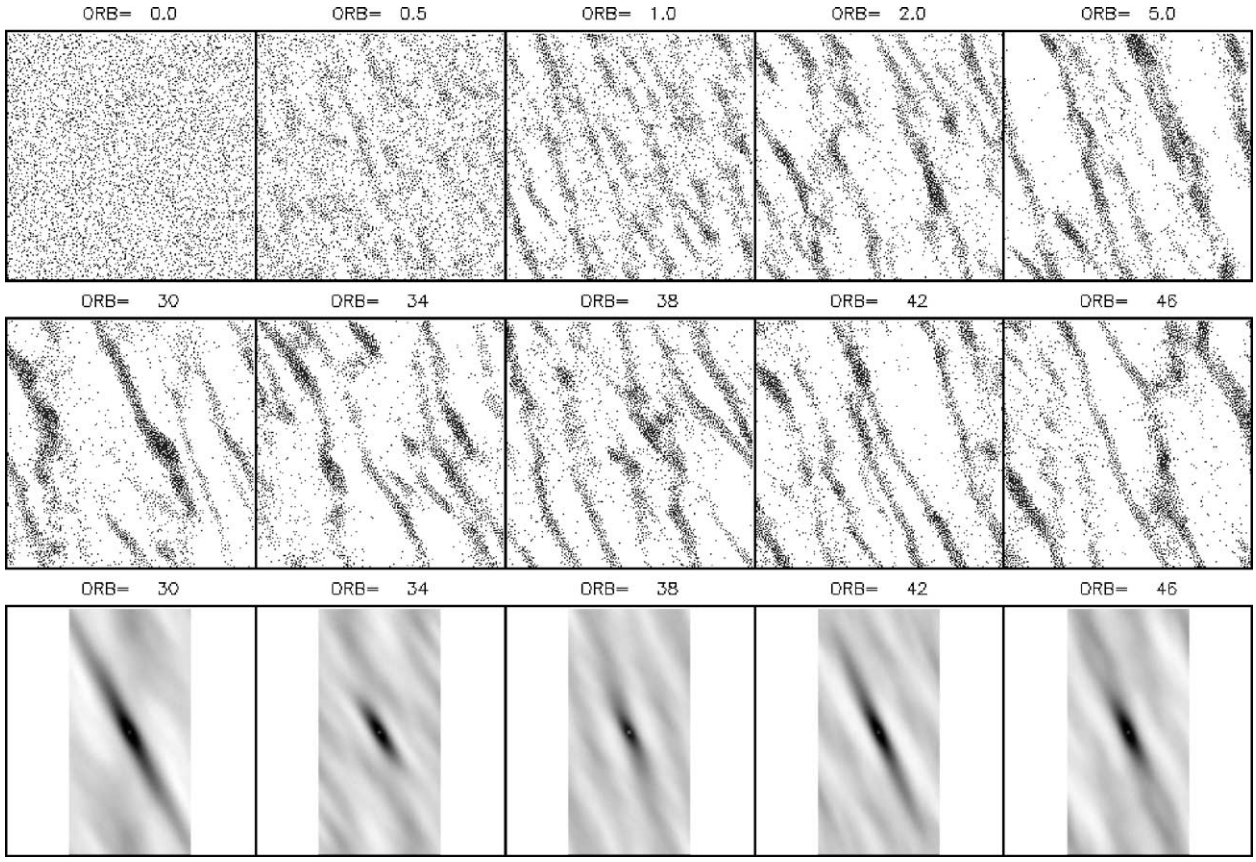

Fig. 2. Time evolution of our standard dynamical simulation model with identical particles. The upper two rows show snapshots from the simulation system, as projected onto the equatorial plane. The planet is to the left and the direction of orbital motion is upward. The run with dynamical optical depth $\tau_{\rm dyn} = 0.5$ is performed for a saturnocentric distance of $a = 130{,}000$ km. Identical particles with radii $r = 1.667$ m, and internal density $\rho = 450\ {\rm kg\,m^{-3}}$ are assumed, yielding a surface density $\Sigma = 500\ {\rm kg\,m^{-2}}$. The Bridges et al. (1984) velocity dependent coefficient of restitution is assumed. The size of the simulation system corresponds to $L_x \times L_y = 4\lambda_{\rm cr} \times 4\lambda_{\rm cr} = 305$ m $\times$ 305 m, and the number of particles is $N = 5300$. The bottom row displays 2D autocorrelation functions for the snapshots corresponding to the middle row.

particle radius set to $r = 1.667$ m, to yield a surface density $\Sigma = 500\ {\rm kg\,m^{-2}}$. For the coefficient of restitution we use the standard velocity-dependent model of Bridges et al. (1984),

$$\epsilon_n(v_n) = \min\left[1, (v_n/v_c)^{-0.234}\right], \tag{6}$$

where v_n is the normal component of the relative velocity of the impacting bodies and the scale parameter v_c equals $v_B = 0.0077\ {\rm cm\,s^{-1}}$ in the Bridges et al. (1984) measurements. For meter-sized particles this elasticity model yields results which are fairly close to using a constant $\epsilon_n \sim 0.5$. In what follows, this run, as well as its counterpart with a power-law size distribution, will be used as our standard dynamical model for producing particle distributions for the photometric calculation of the brightness asymmetry. Note, however, that the strength of the wake structure and the resulting amplitude of asymmetry are sensitive to all these model parameters. For example, using more elastic impacts would weaken the wake structure, which could be compensated by assuming a larger $\tau_{\rm dyn}$, or a somewhat larger ρ. On the other hand, a significantly larger internal density, say $\rho = 900\ {\rm kg\,m^{-3}}$ corresponding to the solid ice density, would increase the tendency of wakes to degrade into gravitational aggregates due to pairwise sticking of particles (Salo, 1992, 1995; Karjalainen and Salo, 2004),[1] which would reduce the resulting brightness asymmetry. The above chosen parameter values thus represent one possible combination which leads to a strong asymmetry at the A-ring distance.

The system followed in Fig. 2 starts with a uniform distribution of particles, with velocity dispersion corresponding to $Q \approx 1$. After one orbital period the system has already divided into small local condensations, with a radial scale of roughly $\lambda_{\rm cr}/2$. These condensations rapidly heat the system, so that Q reaches about 2 after five orbital periods. Simultaneously the scale of the wakes increases. During the later evolution a statistical steady-state between collisional cooling and viscous and gravitational heating is achieved,

[1] In terms of the often employed gravity parameter r_p (see, e.g., Ohtsuki, 1993; Salo, 1995), the summed radius of a particle pair normalized to their mutual Hill radius, the adopted simulation parameters corresponds to $r_p = 1.18$. Since r_p exceeds unity, no gravitational sticking of individual particles is expected, even in the case of zero relative velocity.

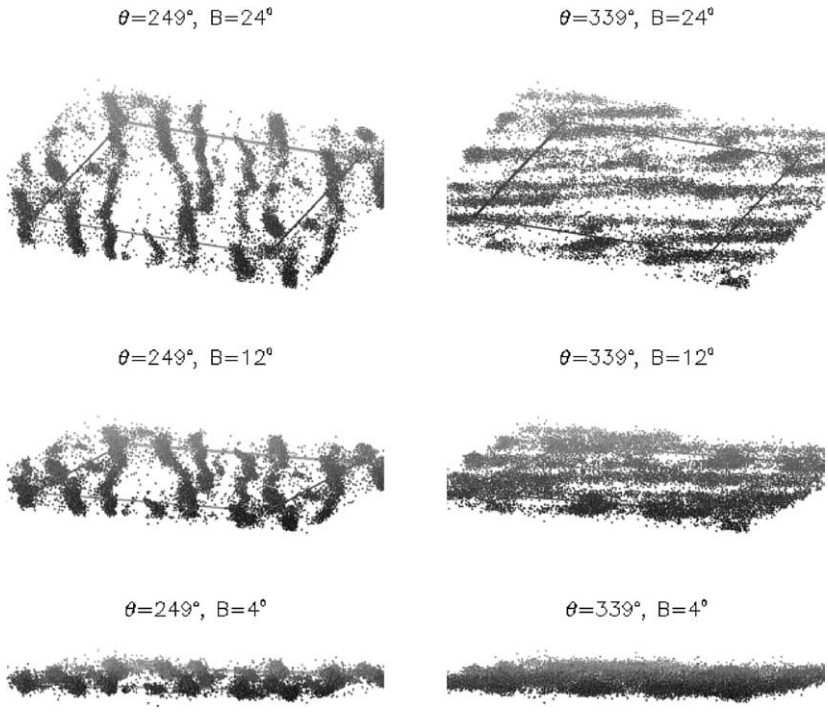

Fig. 3. Dynamical wakes viewed from different directions, providing more quantitative comparison of how the rings might appear locally at the longitudes of expected minimum (left) and maximum (right) brightnesses. Three different elevation angles (B) are illustrated. For a high elevation angle (upper frames), the rarefied regions are roughly equally visible at both longitudes. However, when B is reduced (middle row), a larger portion of rarefied regions is visible in the left-hand frame than in the right-hand frame, indicating azimuthal asymmetry. For very small B, the reflecting areas again become nearly equal, due to imperfect alignment of wakes. Particle positions are taken from the run of Fig. 2 at 42 orbits after the beginning of the simulation. Note that the shading of particles in this plot is not related to their apparent brightness.

so that the average properties of the system (velocity dispersion, wake structure) remain constant, although they exhibit large fluctuations due to the emergence and dissolution of individual strong wakes. More examples are provided in Salo (1995), where several simulations of wake structures were displayed for various surface densities and saturnocentric distances (see also Daisaka and Ida, 1999; Ohtsuki and Emori, 2000). These examples illustrate quite clearly the strong dependence of wake amplitudes on distance, which will be addressed in more detail in our future study.

As seen in Fig. 2, the wakes represent considerable enhancements in density, often having almost empty gaps between them. In the vertical direction the thickness of the wakes is comparable to their radial width. In order to illustrate how such formations may affect the brightness of the ring, Fig. 3 displays one snapshot of the simulation system as it would appear from different viewing directions. Especially for intermediate elevation angles, the fraction of rarefied gaps that are visible depends strongly on the viewing longitude, supporting the simple sketch in Fig. 1.

In the case of a size distribution, the density contrast between wake/inter-wake regions is reduced, as the small particles tend to have a much more uniform distribution than the largest particles. This is illustrated in Fig. 4, for a power-law size distribution of the form

$$dN/dr \propto r^{-q}, \quad r_{\min} < r < r_{\max},\ q = 3. \tag{7}$$

We use $r_{\max}/r_{\min} = 10$ and choose the upper size limit ($r_{\max} = 4.25$ m) in a way which yields the same surface density as the model for identical particles. This distribution is considerably narrower than the size distribution inferred from Voyager radio-occultation measurements (Marouf et al., 1983), with $r_{\max}/r_{\min} \sim 500$ and $r_{\min} \sim 1$ cm. However, the observational size range is fairly model-dependent: for example French and Nicholson (2000) derived a range $r \sim 30$ cm–20 m, based on the amount of forward diffracted light estimated from comparison of Voyager and ground-based occultation experiments. Our truncated model should reveal the qualitative effects of a size distribution, while keeping the required number of particles computationally manageable.

The simulation snapshots in the upper rows of Fig. 2 indicate that the instantaneous direction of wakes is rather variable, making it difficult to estimate very accurately the average orientation of wakes. The same is true for the 2D autocorrelation functions for individual snapshots, calculated as in Salo (1995), displayed in the bottom row of Fig. 2 for the same instants as for which the snapshots of particle positions are displayed in the middle row. However, when averaged over longer time spans (Fig. 5), the characteristic structure of the wakes becomes evident: in the innermost dense part, the average angle is about 25°–30° with respect to local tangential direction, but decreases toward 15°–20° when the tails of the autocorrelation function are considered.

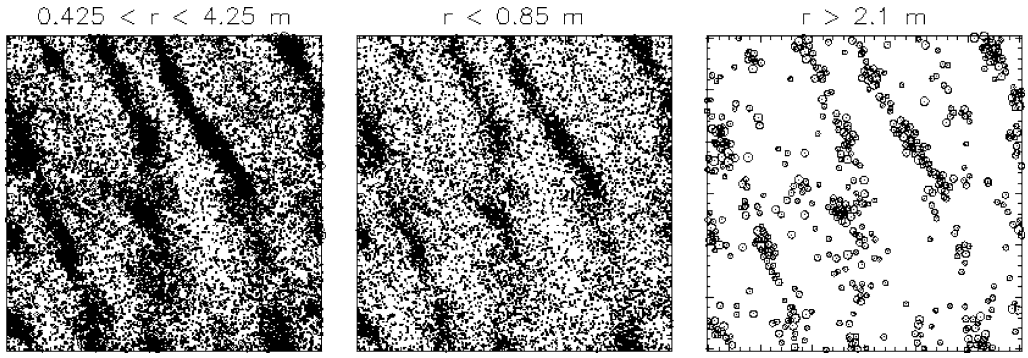

Fig. 4. A typical snapshot from our standard size distribution simulation model. The parameters $\tau_{\rm dyn}$, ρ, a, and $\epsilon_n(v_n)$ are the same as for the model of identical particles in Fig. 2, while here the power-law size distribution is used, with the index $q = 3$, extending from $r_{\rm min} = 0.425$ m to $r_{\rm max} = 4.25$ m, yielding the same Σ as before. In the left-hand frame all particles projected to the central plane are shown, while the other two frames display the particles with $r \leqslant 2r_{\rm min}$ and $r \geqslant r_{\rm max}/2$, respectively. The size of the simulation system corresponds again to $L_x \times L_y = 4\lambda_{\rm cr} \times 4\lambda_{\rm cr} = 305$ m $\times$ 305 m, and the number of particles is $N = 17,500$.

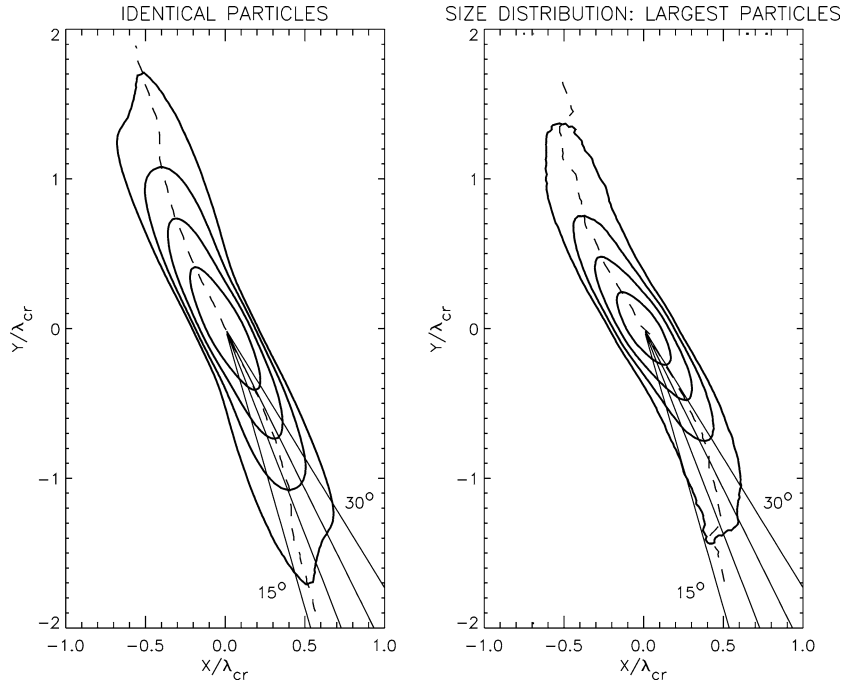

Fig. 5. On the left: the time-averaged 2D autocorrelation function for the run of Fig. 2. The contours display densities at 1.1, 1.25, 1.5, and 2.0 times the ambient density. Solid lines mark directions corresponding to 15°, 20°, 25°, and 30° with respect to the tangential direction, while the dashed curve indicates the loci of maximum density. On the right: the same is shown for the dynamical simulation with a size distribution, using only the locations of the particles with $r > 1.34$ m, comprising one half of total $\tau_{\rm dyn}$.

In the case of a size distribution, the average pitch angle of wakes is larger than that for identical particles. As discussed below, the 2D-autocorrelation function is useful in providing qualitative interpretation for the longitude of minimum brightness found in actual photometric modeling. However, no quantitative results can be derived, as the time-averaged autocorrelation function contains no information of the vertical extent nor the mutual spacing of the adjacent wakes.

2.3. Photometric modeling of wakes

As described in the Introduction, the local wake structure offers a possible explanation for the observed asymmetry, as the effective scattering surface area depends on the direction of viewing with respect to the orientation of the wakes (Figs. 1 and 3). The observed asymmetry can, at least in principle, be used to probe the density contrast due to wake structure, and therefore also the particle properties affecting the formation and strength of wakes (internal density and elasticity of particles). However, detailed photometric modeling is needed for quantitative analysis, addressing the effects of multiple scattering, large volume density, and various observation geometries on the brightness variations corresponding to density variations. Also, the picture is complicated by the fact that the wake structure is most pronounced in the large

particles, whereas the surface area is dominated by the small particles.

In Paper I a Monte Carlo method for determining the photometric properties of arbitrary particle fields was described. The method is based on following a large number of photon paths through successive scatterings on the individual particles until their final escape from the particle system. When combined with an indirect Monte Carlo technique (adding the contributions of individual scatterings on the brightness at a given viewing direction), very good accuracy can be obtained with a computationally manageable number of photons. In order to apply the method to modeling the asymmetry, we assume that the particle positions obtained from dynamical wake simulations sample the typical particle distributions in each ring longitude, in a coordinate system aligned with the local radius vector. For a given viewing geometry, each longitude of the rings has its own illumination and viewing direction for which the brightness is calculated.

Figure 6 illustrates the coordinate system used to model asymmetry. We denote by θ_0 and θ_s the ring-observer and ring-Sun longitude differences, measured in the ring plane in the direction of orbital motion, from the sub-observer and sub-solar points, respectively. Correspondingly, B_0 and B_s stand for the elevation of the observer and Sun with respect to the ring plane in a saturnocentric coordinate system. In the simulation coordinate system, with the x-axis aligned along the local radius vector, the illumination and viewing directions are specified by (ϕ_s, B') and (ϕ_0, B), respectively. For illumination by the Sun, $B' = B_s$ and $\phi_s = -\theta_s$ to a good accuracy. Similarly, in the case of large observing distance (Earth-based observations) $B = B_0$ and $\phi_0 = -\theta_0$. However, in some Voyager observations made from a close range (distance less than a few million kilometers), there is a slight difference. Let $\vec{R}$ denote the saturnocentric radius vector of the studied ring region and $\vec{R}_v$ that of Voyager (in a saturnocentric coordinate system aligned with the coordinate axis of the dynamical simulation),

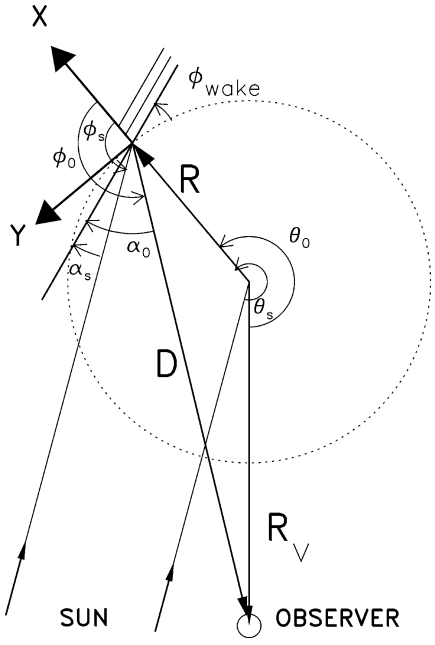

Fig. 6. Coordinate system used in modeling of the asymmetry. $\vec{R}_v$ and $\vec{R}$ represent the saturnocentric radius vectors of the observer and the studied ring region while $\vec{D} = \vec{R}_v - \vec{R}$. θ_0 and θ_s stand for the longitude of the ring region with respect to the sub-observer and sub-solar directions, in the counterclockwise direction (the direction of orbital motion), while ϕ_0 and ϕ_s denote the observer and solar azimuths with respect to the simulation x-axis, aligned with the local saturnocentric radius vector. $\phi_{\rm wake}$ stands for the average angle of the wakes with respect to the local tangential direction (the simulation y-axis), and α_0 and α_s denote the azimuthal viewing and illumination angle with respect to the wakes. For clarity, the elevation angles of the observer and Sun, B_0 and B', are not included in the graph.

$$\vec{R} = \{a, 0, 0\},$$
$$\vec{R}_v = \{\cos\theta_0 \cos B_0, -\sin\theta_0 \cos B_0, \sin B_0\}\Delta, \tag{8}$$

where $\Delta = |\vec{R}_v|$ is the distance of the spacecraft from Saturn's center. The spacecraft direction vector with respect to the ring region is

$$\vec{D} = \vec{R}_v - \vec{R} \equiv \{\cos\phi_0 \cos B, \sin\phi_0 \cos B, \sin B\}|\vec{D}|, \tag{9}$$

from which ϕ_0 and B can be calculated as a function of B_0, θ_0, and a/Δ. When a/Δ is small, we have

$$B = B_0 + \Delta B \approx B_0 + (a/\Delta)\sin B_0 \cos\theta_0,$$
$$\phi_0 = -(\theta_0 + \Delta\theta_0) \approx -\left(\theta_0 + \frac{a}{\Delta}\frac{\sin\theta_0}{\cos B_0}\right). \tag{10}$$

In some of the close-range Voyager images analyzed in Dones et al. (1993), $\Delta/a \approx 10$, so that the maximum shift $|\Delta\theta_0|$ reaches 5°, large enough to be significant in comparison of simulations with observations.

The azimuthal viewing direction α_0 with respect to the major axis of wakes is related to the average pitch angle $\phi_{\rm wake}$ of wakes with respect to the local tangential direction by

$$\alpha_0 = \phi_0 - 90^\circ - \phi_{\rm wake}$$
$$\approx -(\theta_0 + \Delta\theta_0 + 90^\circ + \phi_{\rm wake}). \tag{11}$$

The wakes are viewed most closely along their long axis if $\alpha_0 \approx 0^\circ$ or 180°, corresponding to

$$\theta_0 = 270^\circ - \phi_{\rm wake} - \Delta\theta_0 \quad \text{or}$$
$$\theta_0 = 90^\circ - \phi_{\rm wake} - \Delta\theta_0. \tag{12}$$

For a distant observer, $\Delta\theta_0 = 0$, so that wakes appear edge-on for the longitudes $\phi_{\rm wake}$ before the ansae, as was assumed in Fig. 1. For a nearby observer these longitudes move toward $\theta_0 = 270^\circ$ and away from 90°, as indicated by the sign of $\Delta\theta_0$ in Eq. (10). The azimuthal illumination direction of wakes is similarly

$$\alpha_s = \phi_s - 90^\circ - \phi_{\rm wake}$$
$$= -(\theta_0 + \Delta\theta_s + 90^\circ + \phi_{\rm wake}), \tag{13}$$

where $\Delta\theta_s = \theta_s - \theta_0$ is the difference in sub-solar and sub-observer longitudes. Illumination roughly parallel to wakes

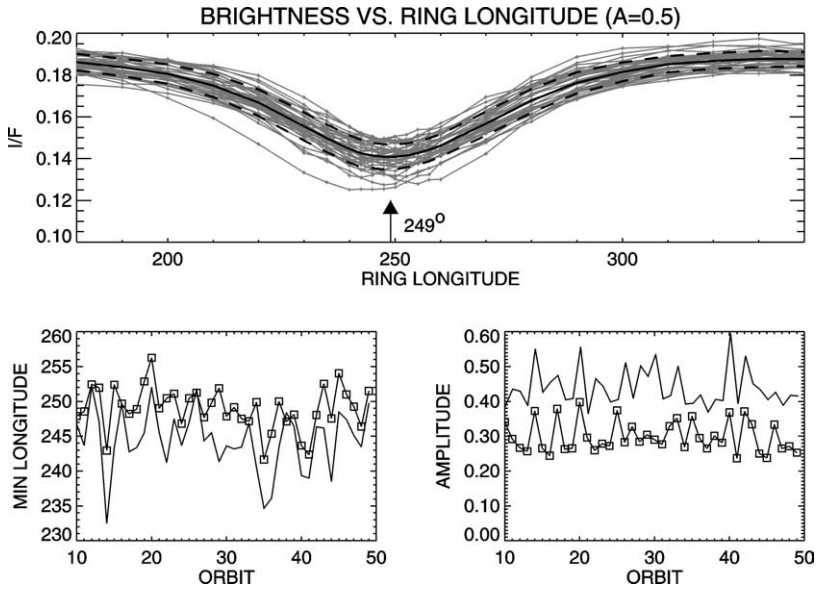

Fig. 7. The upper frame shows the individual brightness vs. ring longitude curves calculated for 40 simulation snapshots of the identical particle run of Fig. 2. Monte Carlo modeling assumes a Lambert phase function and particle albedo $A = 0.5$, observing elevation $B = 12.6°$ and Sun elevation of $B' = 8°$, and $\Delta\theta_s = \theta_s - \theta_0 = 0°$. Infinite viewing distance is assumed. Altogether 25 different ring longitudes were studied, with $N_{\rm phot} = 2 \times 10^4$ photons for each longitude and each snapshot. The thick solid curve is the average I/F curve for all snapshots, while the dashed curves display the $\pm 1 - \sigma$ standard deviation of the individual curves. In the lower frames the symbols connected with lines indicate the modeled longitude of the brightness minimum (left) and the brightness asymmetry amplitude (right) $2(I_{\rm max} - I_{\rm min})/(I_{\rm max} + I_{\rm min})$, for each snapshot separately. For comparison, the curves without symbols show quantities characterizing surface number density autocorrelation functions: the longitude of minimum is compared with $270° - \phi_{\rm auto}$, where $\phi_{\rm auto}$ denotes the major axis direction of the autocorrelation function at the contour level of 1.5 times the ambient density. Similarly, the brightness amplitude is compared to the maximum value of the autocorrelation function at $y/\lambda_{\rm cr} = 1$, multiplied by an arbitrary factor of 0.3. Note that the purpose of these comparisons is to show the qualitative dependence between the density structure and the photometric behavior, not to yield any quantitative estimates.

thus occurs at

$$\theta_0 = 270° - \phi_{\rm wake} - \Delta\theta_s \quad \text{or}$$
$$\theta_0 = 90° - \phi_{\rm wake} - \Delta\theta_s. \tag{14}$$

Two different single scattering phase functions are used in the photometric calculations, determining the scattering probability as a function of phase angle α,

(1) a Lambert phase function

$$P_{\rm L}(\alpha) = \frac{8}{3\pi}\left[\sin\alpha + (\pi - \alpha)\cos\alpha\right], \tag{15}$$

(2) a power-law phase function

$$P_{\rm power}(\alpha) = c_n(\pi - \alpha)^n, \tag{16}$$

defined in Dones et al. (1993): in particular, we adopt $n = 3.092$, $c_n = 0.153$, in which case this function closely approximates the phase curve of Callisto. Both phase functions describe strongly backscattering particles, as appropriate for macroscopic ring particles, the implied anisotropy parameter (see, e.g., Dones et al. (1993) or Paper I) being $g = -\langle\cos\alpha\rangle = -0.44$ and -0.55, respectively.

2.4. Preliminary tests

Since the simulated wakes are transient, time-dependent features, the strength and direction of the wakes and thus also the shape of the modeled brightness vs. longitude curve may be expected to show a large scatter when evaluated at different time steps of the dynamical simulation. Therefore, averages over snapshots from many time steps are employed in the photometric calculations. As long as the sampled time steps are separated by at least the order of one orbital period, no correlation with the previous particle positions is expected. In this sense the time-averaging corresponds closely to the spatial averaging taking place when global properties of ring patches much larger than the size of individual wakes are observed.

Figure 7 displays a representative photometric model, showing the brightness vs. longitude for individual snapshots taken from the dynamical run of Fig. 2. The specific geometry studied corresponds to the Dones et al. (1993) observations of reflected light near the eastern ansa, except that the difference in Sun and Voyager azimuths has been ignored ($\Delta\theta_s = 0°$; also $\Delta\theta_0 = 0°$). Only those portions of the dynamical run are used when the steady-state wake structure has been achieved (after about 10 orbital periods). Although the brightness vs. longitude curve shows considerable scatter between individual time steps, the average curve has a very smooth form. Also shown are the longitude of the modeled brightness minimum, and the asymmetry amplitude, defined in this paper as the full amplitude of brightness variations, normalized by the mean brightness,

$$A_{\rm asy} = 2(I_{\rm max} - I_{\rm min})/(I_{\rm max} + I_{\rm min}), \tag{17}$$

measured for each time separately. These photometric quantities are also compared with the wake direction and strength estimated from the autocorrelation function corresponding to each snapshot. Clearly, there is a similar trend in the photometric values and those characterizing the autocorrelation function. The minimum of the average I/F curve is at $\theta_o \approx 249°$, corresponding to a wake orientation $\phi_{\rm wake} \approx 21°$ with respect to the tangential direction. The average direction of the autocorrelation function depends naturally on the density level studied: comparison to Fig. 5 indicates that the photometric behavior seems to be related to the low density tails of the autocorrelation function (21° corresponds to the direction of contours of the autocorrelation plot at levels of about 1.2 times the average density), which is not surprising for the low viewing elevation studied here ($B = 12°$). For larger viewing elevations the brightness minimum can be expected to move further away from the ansa, since the central parts of the wakes with larger $\phi_{\rm wake}$ will then be more easily visible.

Tests with different numbers of photon, $N_{\rm phot}$, indicate that the main uncertainty of the derived amplitude and the longitude of minimum brightness results from the time variation in wake structure, rather than from the $1/\sqrt{N_{\rm phot}}$ uncertainty intrinsic to the Monte Carlo calculation (see Paper I). For example, the average curves obtained when using only 10^3 instead of 10^4 photons for the same $N_{\rm pos} = 40$ particle snapshots as in Fig. 7 yield practically the same amplitude (within one percent) and longitude of minimum (within 0.1°). The error limits shown in all subsequent plots are therefore calculated from the standard deviation of amplitudes and minimum longitudes obtained for different time steps, divided by $\sqrt{N_{\rm pos}}$, ignoring any formal Monte Carlo errors. The amplitudes themselves, however, are calculated from the maximum and minimum of the combined curves, as well as the minimum longitudes (not from the mean of the amplitudes and minima for individual snapshots, although the difference is small).

In order to compare the simulated wakes to the observed asymmetry, we need to make sure that the size of the dynamical calculation region is large enough to yield an orientation and amplitude of wakes which does not depend too sensitively on the periodic boundary conditions imposed in dynamical simulations, i.e., the size of the calculation region. Since the range of included gravitational forces is limited to a region with a radius $r_{\rm grav} = \min\{L_x/2, L_y/2\}$ around each particle (see Salo, 1995), a larger dynamical simulation region takes into account the interaction of more distant wakes (L_x and L_y denote the full radial and tangential extent of the calculation region, respectively). In Salo (1995) this calculation region dependence was studied in terms of the autocorrelation function, which was found to be nearly constant once the size of the region exceeded about $L_x \times L_y = 4\lambda_{\rm cr} \times 4\lambda_{\rm cr}$ (see also Toomre and Kalnajs, 1991). Figure 8 shows this directly in terms of the minimum longitude and amplitude of the calculated asymmetry, for dynamical runs similar to those in Fig. 2, except for a different size of the calculation region. Indeed the direction of the minimum is found to be rather constant for all runs with $L = L_x = L_y \geqslant 4\lambda_{\rm cr}$, in agreement with the autocorrelation function being almost constant. The asymmetry amplitude, however, seems to decline slightly with $L/\lambda_{\rm cr}$ even beyond this. The effect is fairly small and is likely to result from the fact that the total gravitational effect of wakes is slightly overestimated when only a few first wavelengths are included in the force calculation. However, since for a fixed $\tau_{\rm dyn}$ and Σ the particle number grows in proportion to L^2, the CPU time consumption in such large $L/\lambda_{\rm cr}$ dynamical runs becomes very large. As a compromise we perform all our models with $4\lambda_{\rm cr}$ by $4\lambda_{\rm cr}$ simulation regions, which are likely to yield correct amplitudes within a few percent.

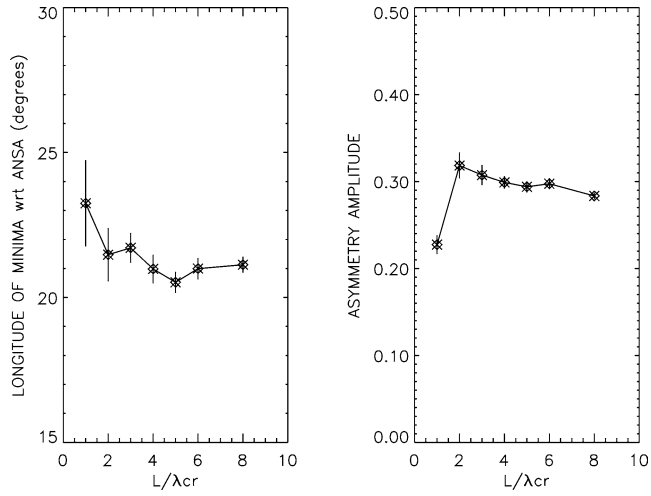

Fig. 8. The dependence of modeled brightness asymmetry on the size of the dynamical simulation region. Different runs with the same parameter values as in Fig. 2 are compared, for different sizes of the square-size calculation region (and correspondingly different numbers of particles). Parameters for the photometric calculations are the same as in Fig. 7. The error bars correspond to ±1 standard deviation of the values calculated for individual snapshots, divided by $\sqrt{N_{\rm pos}}$, where $N_{\rm pos} = 40$ is the number of snapshots.

Finally, we also performed some additional checks of the photometric method when applied to modeling of wakes, in addition to the tests already described in Paper I. For example, the results of photometric calculations were found to be unaffected if the size of the modeled particle field was doubled, by including the appropriate copies of the particles implied by the periodic boundary conditions among the actual simulation particles themselves (note that this is different from changing the size of the original region in dynamical simulations). Since any error in the treatment of boundaries is likely to become much more pronounced in the case of inclined wakes than in the case of spatially homogeneous particle systems studied in Paper I, this provides an additional confirmation of the correct treatment of particle replicas in terms of image photons, as described in Paper I.

3. Comparison to observations

In this section we compare the predictions of dynamical simulations to the azimuthal asymmetry seen in Voyager observations of reflected and transmitted light. We also demonstrate that the tilt-angle dependence of the asymmetry amplitude found in ground-based observations has a simple interpretation in terms of wakes. For these comparisons the two standard dynamical runs of the previous section for identical and size distribution model are used for producing the photometric models.

3.1. Brightness asymmetry in reflected and transmitted radiation

In Dones et al. (1993) the azimuthal dependence of the A ring brightness was analyzed from a series of close-range Voyager 2 images of the eastern ansa. Due to the small phase angle ($\alpha = 13°$) the contribution from Saturn shine is negligible for strongly backscattering ring particles. According to these observations the brightness has a well-defined minimum near $\theta_0 = 249°$. In addition the observed minimum is asymmetric, in the sense that the brightness increases more rapidly for $\theta_0 < 249°$ than for $\theta_0 > 249°$. Figure 9 compares the modeled asymmetry with the observations shown in Fig. 19 in Dones et al. (1993). Except for the difference of a few degrees in the minimum longitude, the overall brightness level and its variations are well reproduced in the model with identical particles, when using reasonable values for particle albedo and phase function ($A \approx 0.43$ for a power-law phase function approximating Callisto's phase curve). Also shown in the plot is the contribution due to single scattering alone, indicating that the shape of the curve is determined by single scattering, and is thus not very sensitive to the assumed phase function: a Lambert phase function with $A \approx 0.65$ would yield practically identical results. On the other hand, our model with a size distribution yields about a factor of two smaller amplitude, and the minimum is even further away from the ansa than is observed.

The modeled minimum brightness longitude in Fig. 9 differs from that in Fig. 7, which yielded 249° in the case of equal illumination and viewing azimuths, for the same B and B'. This shift follows from the $\Delta\theta_s = 10.2°$ difference in the Sun and observer longitudes,which is taken into account in the model curve of Fig. 9. Also the shift $\Delta\theta_0 \approx -2.2°$ is included, see Eq. (10). In fact, the modeled minimum brightness seems to fall very close to the mean of the longitudes corresponding to the viewing and illumination along the average long axis of wakes, which according to Eqs. (12) and (14) indicates

$$\theta_0 = 270° - \phi_{\text{wake}} - \frac{1}{2}\Delta\theta_s - \frac{1}{2}\Delta\theta_0 \approx 270° - 21° - 5.2° - (-1.1°) \approx 245°, \quad (18)$$

for an intrinsic wake pitch angle $\phi_{\text{wake}} \approx 21°$. This difference in illumination and viewing directions may also account for the asymmetric shape of the minimum. This asymmetry is present in the model curve of Fig. 9, although it is

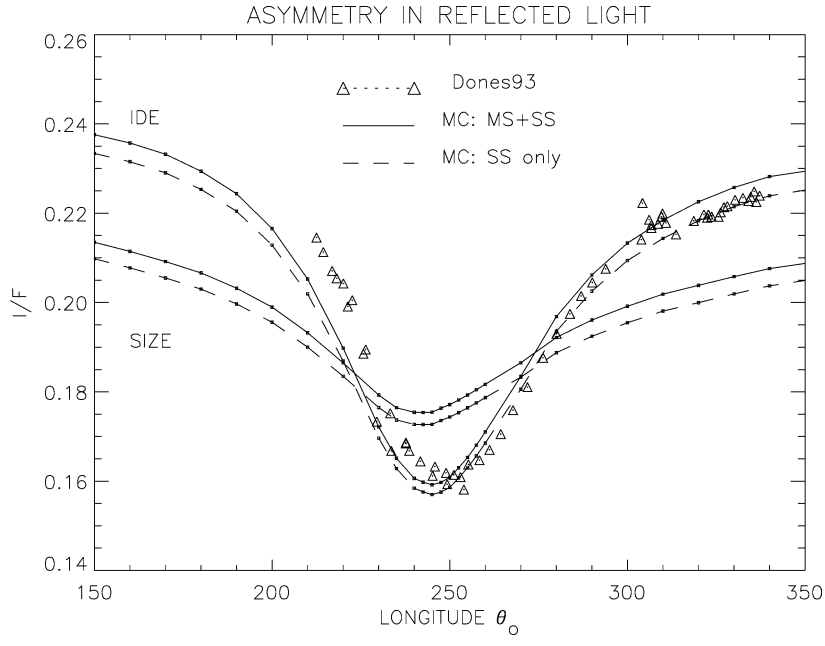

Fig. 9. Observed shape of the asymmetry at the distance of 128,000 km, as seen in Voyager 2 images at phase angle $\alpha = 13°$, with Voyager elevation $B = 12.6°$ and Sun elevation of 8° (Dones et al., 1993). Also shown is the modeled curve for the dynamical simulation of Fig. 2. We have taken into account the finite distance of the spacecraft from the rings ($\Delta = 3.3 \times 10^6$ km), and used $B_0 = 12.8°$ as the Voyager latitude with respect to the ring plane while $\theta_s - \theta_0 = 10.2°$, yielding the same values for B and α as listed for various θ_0 values in Table III in Dones et al. (1993). For this case the maximum shift in viewing azimuth due to the proximity of the spacecraft to the rings amounts to $\Delta\theta_0 \approx 2.2°$. A power-law phase function approximating Callisto's phase curve is used, with $A = 0.43$. The single-scattered contribution is shown separately. Both the standard dynamical models for identical particles and for a size distribution are used.

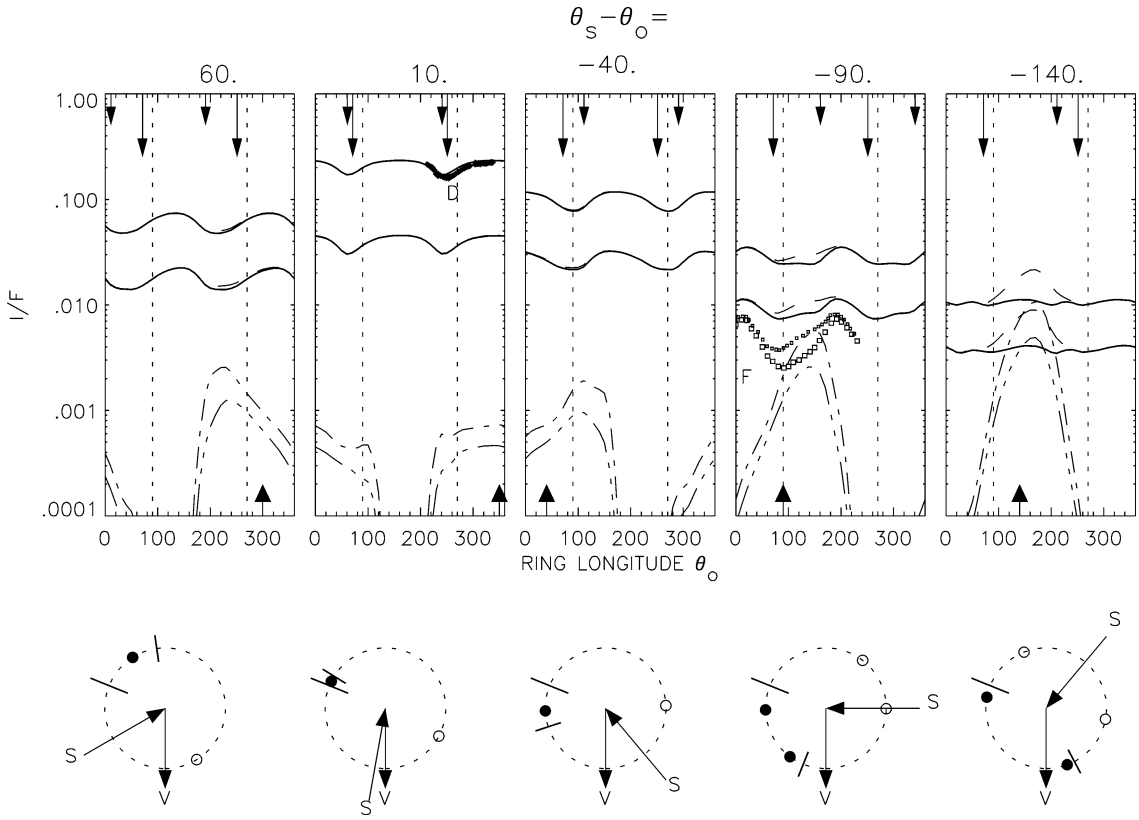

Fig. 10. The modeled brightness vs. ring longitude for different solar directions with respect to the observer, $\theta_s - \theta_0$, using the standard dynamical model for identical particles. The solar elevation angle is fixed at $B' = 8°$ and infinite viewing distance is assumed. The upper solid curves show the modeled brightness for observing elevation $B = 12.6°$, while the lower solid curves correspond to transmitted radiation at $B = -29°$. A Callisto phase function with $A = 0.43$ is used. The dash-dotted curves stand for the contribution of Saturn-shine, calculated with Barkstrom's law (Barkstrom, 1973), using numerical factors interpolated from the values tabulated in Table V in Dones et al. (1993) (average over zones and belts in blue, Saturn's oblateness is ignored). The upper and lower curves again correspond to $B = 12.6°$ and $B = -29°$, respectively. The dashed curves (above the solid curves, as seen in frames for $\theta_s - \theta_0 = -90°$, $-140°$ and $60°$) indicate the combined solar and Saturn-shine. The long (short) arrows extending from the upper x-axis indicate the ring longitudes where the wakes are viewed (illuminated) roughly perpendicularly, $\alpha_0 = 0°$ ($\alpha_s = 0°$), while the arrows extended from the lower x-axis indicate the solar longitude. The points in the frame for $\theta_s - \theta_0 = 10°$ denote observations by Dones et al. (1993) (labeled by "D") and those in the frame for $\theta_s - \theta_0 = -90°$ stand for observations of Franklin et al. (1987) (labeled by "F"), both with and without Saturn-shine (data points from Franklin et al. (1987), Fig. 5d, scaled by an arbitrary factor). The geometry is also depicted in the lower frames: the filled circles stand for the local minima in modeled brightness, while long and short ticks mark the longitudes corresponding to viewing ($\alpha_0 = 0°$) and illumination ($\alpha_s = 0°$) along the wakes, respectively. Open symbols stand for the other symmetrically located minima.

somewhat weaker than in the observations. By contrast, note that the brightness profile in Fig. 7 for $\Delta\theta_s = 0°$ is completely symmetric. The larger shift of the minimum from the ring ansa for the size distribution model follows directly from the larger pitch angle of wakes, as anticipated based on the autocorrelation plots in Fig. 5.

The effect of the illumination direction on the location of the minimum, as well as on the asymmetric shape of the minimum, becomes more evident in Fig. 10, where the upper curves display the modeled asymmetry vs. longitude in a series of runs again with $B' = 8°$ and $B = 12.6°$ as in the Dones et al., Fig. 19, observations, but with varied $\Delta\theta_s$. In each frame the arrows indicate the directions corresponding to $\alpha_0 = 0°$ or $180°$ (long arrows extending from the upper x-axis) and to $\alpha_s = 0°$ or $180°$ (short arrows extending from the upper x-axis). Clearly, both these directions seem to be related to a local minimum brightness, the influence of illumination being stronger on the combined minimum. In particular, comparing the frames with $\Delta\theta_s = 60°$ and $-40°$, one sees that the brightness gradient is in both cases steeper for the side corresponding more closely to parallel illumination. Most likely this follows from the fact that observations have $B' < B$ (Dones, 2003, personal communication). Indeed, in the case of larger solar elevation, $B' > B$, the asymmetry of the minimum should be reversed, as confirmed in additional experiments with $B' = 20°$ instead of $8°$. For well-separated illumination and viewing, $\Delta\theta_s = -90°$, the minimum becomes very wide and even divides into two local minima, one being close to the parallel illumination of wakes and the other close to the parallel viewing.

Also shown in Fig. 10 (lower curves) is a set of model curves for transmitted light with $B' = 8°$, $B = -29°$. Although the overall brightness level is now much lower than in reflected light, the relative brightness variations have a similar longitude dependence. Also shown in the plot, for $\Delta\theta_s = -90°$, is the observed curve in transmitted light

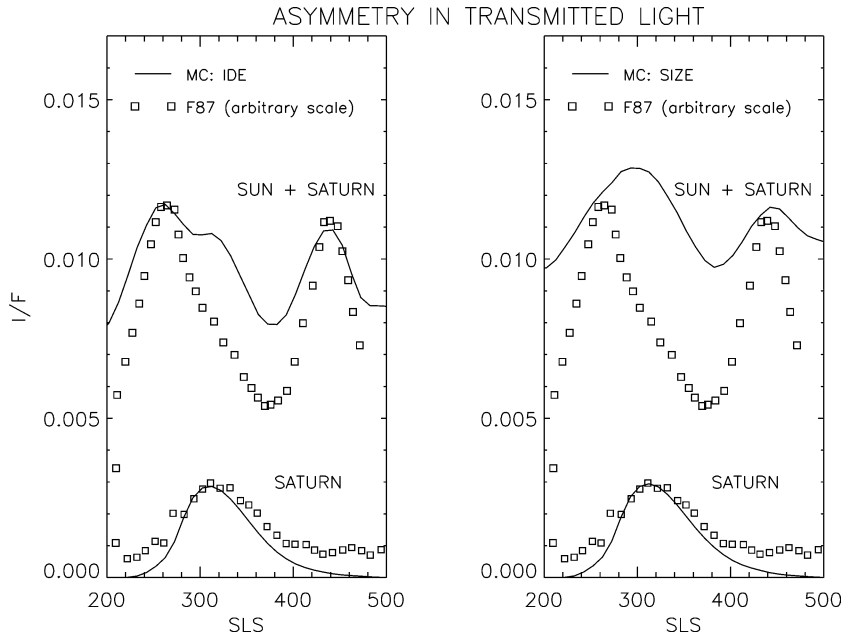

Fig. 11. A more detailed comparison with the observed asymmetry in transmitted light. Symbols denote the Franklin et al. (1987) measurements of the Voyager 2 image FDS 44169.26, for $a = 127{,}000$ km, $B = -28.8°$, $B' = 8.1°$, $\theta_s - \theta_0 = -90°$, traced from their Fig. 5d. The SLS longitude system is used, where SLS $= 92.4° - \theta_0$. Besides the total observed I/F, the amount of Saturn-shine estimated in Franklin et al. (1987) is displayed. Model curves (for both Saturn-shine and Saturn-shine + transmitted solar radiation) are calculated using a Callisto phase function with $A = 0.43$, both with the standard dynamical run for identical particles and for a size distribution. Original observations given in digital units are scaled by multiplication with an arbitrary factor.

(from Fig. 5d in Franklin et al. (1987), with an arbitrary intensity scale). The contribution from Saturn-shine is also shown (dashed lines), since it is important near the minimum analyzed by Franklin et al. (1987). A more detailed comparison to their observations is shown in Fig. 11. Altogether, although the modeled fractional amplitude is somewhat smaller than the observed one, the location of the minimum is well accounted for. Again, the model with identical particles agrees better with observations than the model with a size distribution.

The fact that a very similar longitude dependence is seen in both reflected and transmitted light is related to the large elevation angles studied in Fig. 10. In this case the brightness in transmitted light seems also be determined mainly by the fraction of scattering area, just as for the reflected radiation. However, as discussed in Franklin et al. (1987), for small α and low elevation angles one would expect a reversal of brightness minima and maxima between transmitted and reflected radiation, basically because only the low-density inter-wake regions transmit any light at all, and these are shadowed by the wakes except for viewing very nearly along the long axis of the wakes. Indeed, when the models of Fig. 10 are extended to smaller B and $|B'|$, such a reverse behavior is obtained (Fig. 12). For example, when $B = 8°$ and B' is slightly negative and $\theta_s \sim \theta_0$, there is a *maximum* in transmitted light near $\theta_0 = 250°$, which changes into a local minimum when $|B'| > 4°$. For still lower viewing elevation ($B = 3°$) the local maximum persists for somewhat larger $|B'|$, and I/F becomes almost independent of longitude for $B' = -16°$ if $\theta_s - \theta_0 = 0°$. In this case the effects of even very small non-zero $\theta_s - \theta_0$ are very pronounced, the minimum and maximum I/F being very sensitive to the exact geometry. For comparison, Fig. 12 also displays the reflected radiation at similar low elevations, showing no qualitative changes in comparison to larger elevations (for $B = 3°$, $B' = 2°$ the larger I/F for $\theta_s - \theta_0 = 0$ in comparison to $-10°$ or $10°$ reflects the opposition brightening).

3.2. Brightness asymmetry at different elevation angles

Ground-based observations (Lumme and Irvine, 1976a, 1979b; Lumme et al., 1977; Thompson et al., 1981) indicate that the asymmetry amplitude increases when $B \approx B'$ decreases from 26° to 12°, while for still smaller elevations the amplitude again decreases (Thompson, 1982). Also the width of the asymmetry minimum shows signs of becoming more narrow for smaller elevations (Lumme and Irvine, 1976a). This qualitative tilt-angle dependence of the asymmetry is naturally accounted for by the wake model (see Fig. 3). Since the vertical extent of wakes is smaller than their radial separation, for large B the scattering area varies only little with the azimuthal viewing angle with respect to the wakes' major axis direction. With decreasing elevation the shielding of rarefied regions becomes increasingly effective for nearly perpendicular viewing azimuths. However, for very small elevations the gaps are completely hidden from any direction, since the wakes are not perfectly straight. Figure 13 illustrates these effects more quantitatively, in terms of the modeled I/F vs. θ_0 for different elevations.

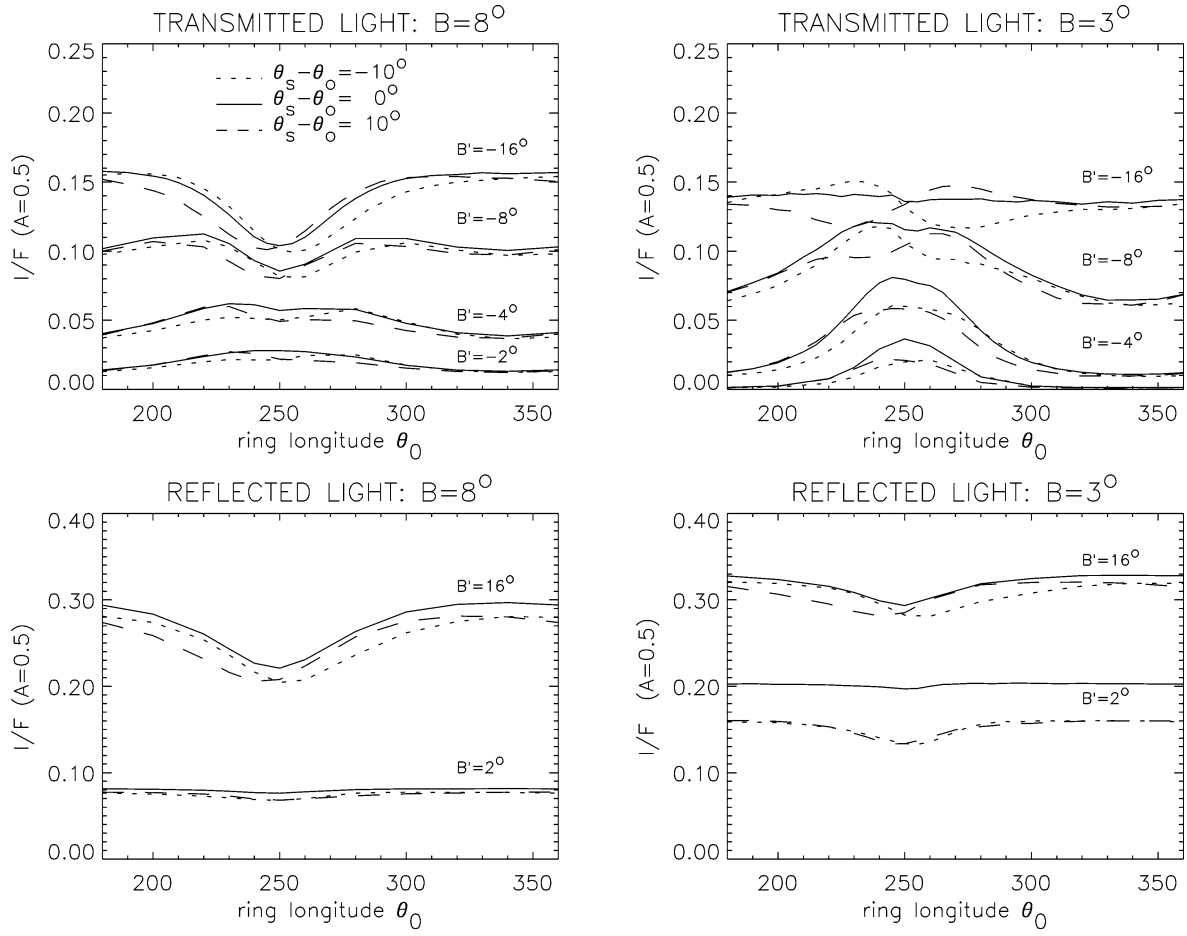

Fig. 12. Modeled asymmetry in transmitted and reflected light for low elevations. In the upper frames the brightness vs. ring longitude is shown for $B = 8°$ and $B = 3°$, for different solar elevations. A Lambert phase function with $A = 0.5$ is used. For sufficiently small $|B'|$ and $|B|$ the ring longitude where viewing is along the wakes may appear as a brightness maximum in transmitted light, contrary to the case of transmitted light for larger elevation angles (see Fig. 10), or for the case of reflected light (lower frames). Also indicated is the influence of small changes in $\theta_s - \theta_0$. The dynamical model for identical particles is used.

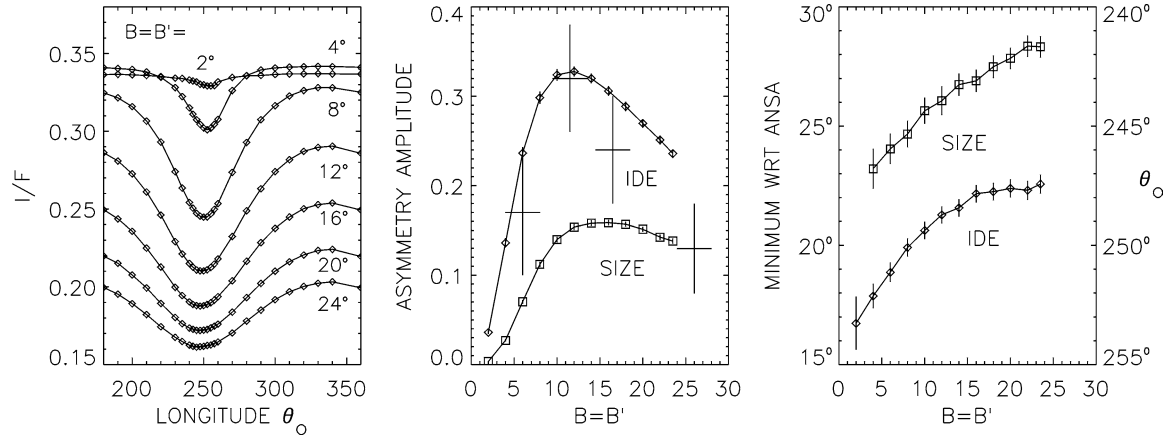

Fig. 13. The dependence of asymmetry on tilt angle. On the left, brightness vs. elevation is shown for photometric simulations performed for various elevation angles. The dynamical simulation data correspond to the standard model with identical particles. Photometric runs are performed for $\alpha = 0°$ and $B = B'$, using a Lambert phase function and $A = 0.5$. In the middle frame the asymmetry amplitude (Eq. (17)) is shown, both for the runs shown on the left frame, as well as for corresponding models using the standard size-distribution simulation. Large symbols with error bars show observations by Thompson (1982) (Table 3, blue light for $\alpha < 1°$). The right frame shows the longitude of modeled minimum brightness with respect to ansa; the axis labels in the right show the same in terms of ring longitude θ_0.

In general, comparison to ground-based observations (Thompson, 1982) shows a good qualitative agreement in the asymmetry amplitude, the observations falling between that implied by photometric models for our standard dynamical run with identical particles and with a size distribution. In addition, in agreement with observations the width of the modeled minimum is reduced for small elevations, as may be expected since the wakes must be viewed more and more precisely along their long axis for the gaps to be visible. The figure also indicates the large reduction of the amplitudes obtained in the case of a size distribution, in agreement with the models shown in Fig. 9, resulting from the tendency of small particles to fill the rarefied gaps to some degree. The direction of modeled minimum longitude shows also a clear tendency of being shifted away from ansa for the larger elevations. A likely explanation is that for higher elevations the brightness is becoming increasingly dominated by the inner parts of the wakes: the autocorrelation plots of Fig. 5 indicate that the central parts of wakes make on average a larger angle with respect to the tangential direction than the tails which dominate for more shallow viewing directions. Also, there is a clear difference in the longitude of minimum brightness between models with identical particles and with a size distribution, the latter models yielding a minimum further away from the ansa. This is also consistent with the differences in the autocorrelation function.

3.3. Role of multiple scattering

As discussed in relation to Fig. 9, the modeled asymmetry is dominated by single scattering. Nevertheless, the higher orders of scattering exhibit a rather similar brightness vs. longitude dependence, with even higher fractional amplitude. This is illustrated in Fig. 14, for the elevation angle of 10° yielding near-maximal asymmetry amplitude; practically identical behavior is obtained for both Lambert and Callisto phase functions. Since the fractional contribution of multiple scattering increases with albedo, the expected asymmetry amplitude will also increase. A similar conclusion results from Lumme and Irvine (1979a) model based on multiple scattering in optically thick blobs. However, since the overall contribution of multiple scattering is fairly small in our models (see Fig. 9), the expected magnitude of this effect is not very large. This is shown in Fig. 15, indicating that for the geometry of Fig. 14 the amplitude varies by at most about 15% for different values of albedo. For a Callisto phase function the maximal difference is smaller than for a Lambert phase function, because its more backscattering character leads to a larger relative contribution of single scattering at small phase angles. This model result, the increase of asymmetry amplitude with albedo, is qualitatively consistent with the observations reported in Lumme et al. (1977). According to their observations for an elevation angle of about 16°, the amplitude of asymmetry in red light (effective wavelength $\lambda_{\text{eff}} = 590$ nm) appeared even 50% larger that in blue light ($\lambda_{\text{eff}} = 415$ nm). Such a dependence

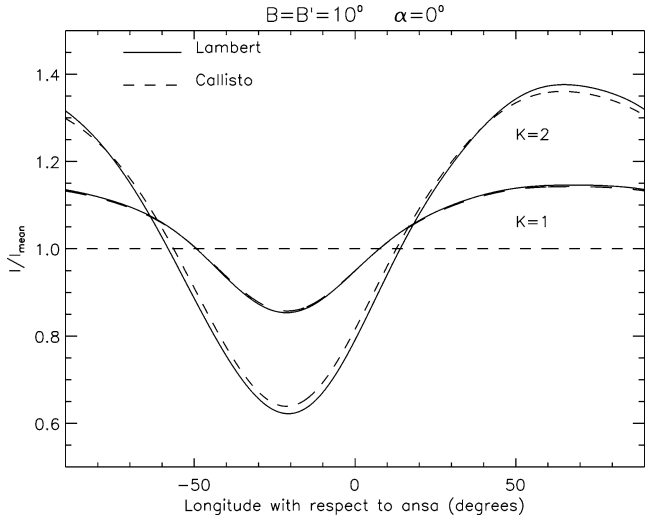

Fig. 14. Comparison of asymmetry profile in first ($k = 1$) and second ($k = 2$) order scattering. In each case, the curve is normalized by $I_{\text{mean}} = \frac{1}{2}(I_{\max} + I_{\min})$, calculated for the order studied. For clarity, the higher orders are not shown: in $k = 3$ the amplitude is slightly smaller than that for $k = 2$, while for $k \geqslant 4$, the amplitude is even bigger than for $k = 2$. Photometric simulations for the identical particle model, with $B = B' = 10°$, zero phase angle are shown; a similar stronger amplitude in higher order scatterings is also seen for other elevation angles.

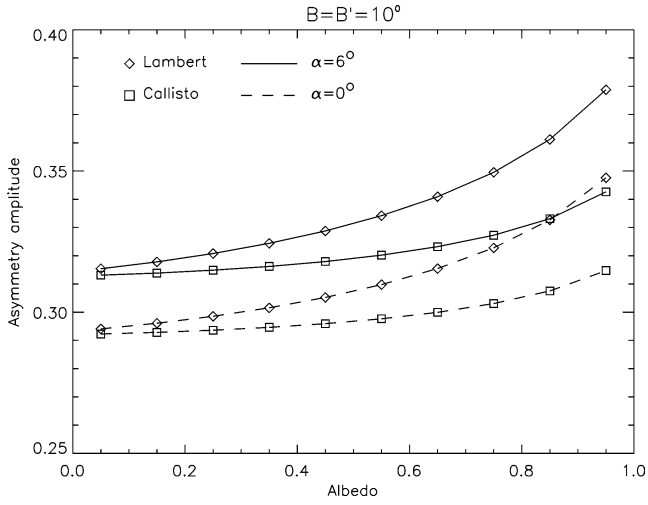

Fig. 15. Dependence of asymmetry amplitude on albedo and phase function. Photometric simulations for the identical particle model, with $B = B' = 10°$, are shown, both for $\alpha = 6°$ and $\alpha = 0°$. The increased overall amplitude of a Lambert phase function in comparison to a Callisto phase function follows from the larger contribution of multiple scattering in the former case, which, according to Fig. 14, exhibits a stronger relative variation than the singly-scattered component. On the other hand, the reduced opposition amplitude reflects the decrease in the variations of the singly-scattered flux, taking place in a similar fashion regardless of the phase function.

on wavelength was confirmed in their later analysis including smearing corrections (Thompson et al., 1981), although its exact magnitude was difficult to estimate due to observational uncertainties.

Figure 15 also compares the amplitudes for phase angles $\alpha = 6°$ and $\alpha = 0°$, indicating that for both studied phase

functions the asymmetry amplitude is reduced by about 10% at opposition. Since this reduction is not sensitive to the assumed albedo, it must be a single scattering effect. Near opposition, the singly scattered flux increases, due to reduced mutual shadowing between particles (see Paper I and references therein). The reduced asymmetry amplitude indicates that this brightening is more important at brightness minima, compared to that in longitudes yielding a brightness maximum. A likely reason is that the opposition brightening becomes stronger with the path optical depth (see Paper I), having thus the largest importance in viewing along the long axis of the dense wakes (corresponding to minimum brightness). The reduction of opposition amplitude is also qualitatively consistent with the observations in Lumme et al. (1977), who found significantly reduced asymmetry amplitude in their observations for $\alpha = 0.11°$ in comparison to $\alpha \sim 1°$. Again, this result was at least marginally confirmed in the later analysis in Thompson et al. (1981).

3.4. Optical depth

Our dynamical models use fixed $\tau_{\rm dyn} = 0.5$, defined as the total surface area of particles divided by the area of the calculation region,

$$\tau_{\rm dyn} = \int_{r_{\rm min}}^{r_{\rm max}} \pi r^2 \, dN(r), \tag{19}$$

where $N(r)$ is the number density of various-sized particles. On the other hand, the photometric optical depth along a given direction is defined by

$$\tau_{\rm path} = -\log(f_{\rm path}), \tag{20}$$

where $f_{\rm path}$ denotes the fraction of light passing through the layer in that direction. In the case of a geometrically thick, spatially homogeneous, low-volume-density ring ($D \to 0$), $\tau_{\rm path}$ is proportional to the geometric path length, so that the perpendicular photometric optical depth,

$$\tau_{\rm phot} = \tau_{\rm path}(B) \sin B, \tag{21}$$

is independent of elevation B, and equals $\tau_{\rm dyn}$. In Paper I we found that generally $\tau_{\rm phot} > \tau_{\rm dyn}$ for spatially homogeneous systems, the enhancement increasing with the volume filling factor D, consistent with Esposito (1979) and Peltoniemi and Lumme (1992). On the other hand, $\tau_{\rm phot}$ was found to be practically independent of B as long as the vertical thickness of the layer was at least a few particle diameters.

In the case of spatially inhomogeneous rings, $\tau_{\rm phot}$ derived via Eq. (21) is expected to depend on B, as suggested by Hämeen-Anttila and Vaaraniemi (1975) in their ring models including narrow ringlets separated by low density gaps. In such a case, the amount of light passing through the ring depends mainly on the fractional area and optical depth of rarefied gaps. The same is also true in the case of gravity wakes. In addition, since the visibility of gaps depends on the direction of the light ray with respect to the local wake direction, the derived $\tau_{\rm phot}$ will depend on both B and θ_0. This is illustrated in Fig. 16, showing the $\tau_{\rm path}(B, \theta_0)\sin(B)$ profiles for the same models whose brightness was shown in Fig. 13. Indeed, the ring longitudes which correspond most closely to the minimum brightness (direction of wakes) appear also as minima for $\tau_{\rm phot}$ if defined as above in Eq. (21). Moreover, this minimum value increases monotonically with B, due to the $\sin B$ factor, as $\tau_{\rm path}$ mainly measures the fraction of gaps through $f_{\rm path}$ and varies only little with B. However, $\tau_{\rm path}(B, \theta_0)\sin(B)$ does not go to zero for $B \to 0°$, due to the finite vertical extent and the imperfect alignment of the wakes, and the non-zero particle density in the gaps. Similarly, the maximum $\tau_{\rm phot}$ corresponds to perpendicular viewing with respect to wakes. The maximum $\tau_{\rm phot}$ varies

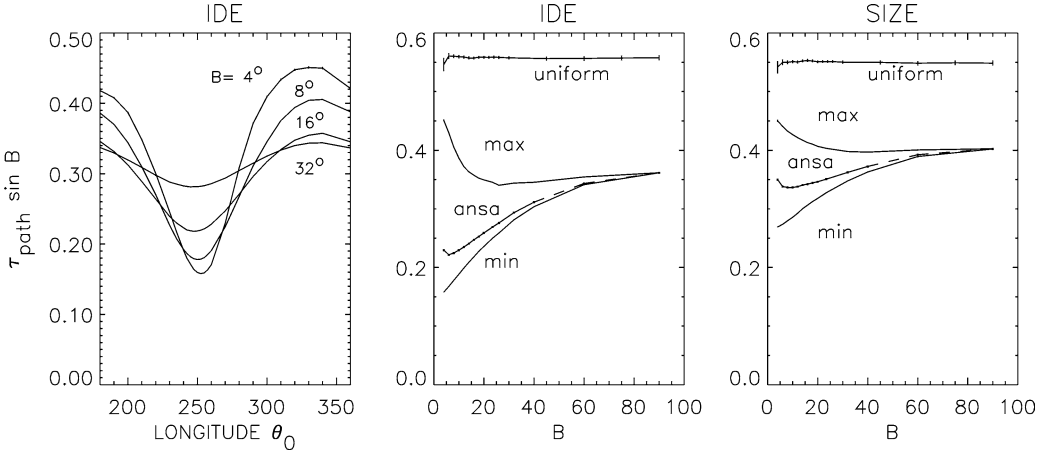

Fig. 16. The dependence of photometric optical depth on the viewing direction. At left the optical depth profiles as a function of ring longitude are shown for different elevations, using the standard dynamical run for identical particles. In each case the path optical depth is converted to normal optical depth in the manner typically assumed for a spatially homogeneous low volume density ring ($\tau_{\rm phot} = \tau_{\rm path} \sin B$). In the middle, the maximum and minimum optical depths are shown as a function of elevation, as well as the optical depth corresponding to the ansa. At right the same is shown for the standard size distribution model. For comparison the optical depths are also shown for similar models using dynamical data from runs where self-gravity is not included ('uniform'). In each case $\tau_{\rm dyn} = 0.5$.

less with B, except that it starts to rise for small B. This indicates that $\tau_{\rm path}$ across the wakes increases with longer path length, although not in the same manner as for a uniform ring. At large B the minimum and maximum $\tau_{\rm phot}$ approach a common value, which, however, is clearly smaller than $\tau_{\rm dyn}$. In the case of a size distribution, the overall $\tau_{\rm phot}$ is larger than for identical particles (but still less than $\tau_{\rm dyn}$), due to the small particles having a more uniform spatial distribution, reducing the effect of rarefied regions. Also, the sensitivity to B and θ_0 is reduced, but remains still significant.

For comparison, Fig. 16 also shows the $\tau_{\rm phot}$ vs. B dependence in the case of dynamical runs similar to our identical particle and size distribution models, except that the self-gravity of particles has been ignored (labeled as 'uniform'). In these models $\tau_{\rm phot}$ exceeds $\tau_{\rm dyn}$ by about 10%, consistent with their significantly non-zero D (the central plane filling factors are about 0.125 and 0.145 for the model with identical particles and the model with a size distribution, respectively) (see Paper I).

3.5. *Inverse tilt-effect*

Ground-based observations indicate that the brightness of the B ring increases ("tilt-effect") with elevation angle, by about 25% between $B = B' = 6°$ and 26°, whereas the brightness of the A ring is constant within about 10% (Lumme and Irvine, 1976b). In Lumme et al. (1983) the B ring tilt effect was interpreted in terms of increased multiple scattering with increasing elevation, this effect being less significant for the A ring because of its smaller optical depth. Moreover, in Paper I we showed that the B ring tilt effect could also be explained by its large central plane volume density, combined with the size distribution and vertical distribution of particles: for increasing elevations the dense central portions, appearing relatively brighter because of their opposition brightening, would become increasingly visible, leading to enhanced brightness. Again, this brightness effect would be less significant for the A-ring. However, due to limited radial resolution, these ground-based measurements (Lumme and Irvine, 1976b) for the A ring referred just to the brightest, innermost A ring. The recent analysis of HST images (Cuzzi et al., 2002) shows the full brightness profiles of rings vs. distance and confirms the general trend, i.e., the strong increase of brightness with elevation for the B ring and a smaller increase for the innermost A ring. However, their analysis also indicates that for the A ring at $a = 125{,}000$–$130{,}000$ km, the brightness in fact *decreases* with elevation angle, suggesting that this region is effectively optically thin. Most interestingly, this decrease is even stronger than the slight reduction expected in the singly scattered component, calculated for the A ring optical depth in these regions ($\tau_{\rm phot} \sim 0.45$). Since this region with exceptional behavior coincides with the region where the strongest asymmetry is seen, it is of interest to check whether this "inverse tilt effect" could be explained by the presence of gravity wakes. Indeed, signs of such an effect were seen in Fig. 13, suggesting that in the presence of strong wakes, the overall brightness decreases with elevation.

A more detailed study is shown in Fig. 17, in terms of the same quantities shown in Cuzzi et al. (2002)'s Fig. 8, namely the brightness at the ring ansa, for a phase angle $\alpha = 6°$. Photometric models for dynamical simulations without self-gravity are also shown (labeled by "ng"), to emphasize the difference as compared to the case where wakes are not present. In the left-hand frame the brightness I/F vs. elevation angle is shown, as well as the theoretical single-scattering brightness for uniform rings with volume density $D \to 0$,

$$\left(\frac{I_{\rm ss}}{F}\right)_{\rm refl} = \frac{A\,P(\alpha)\mu_0}{4(\mu+\mu_0)}\left(1-\exp\left[-\tau(1/\mu+1/\mu_0)\right]\right), \quad (22)$$

where $\mu_0 = |\sin B'|$ and $\mu = |\sin B|$. In the construction of theoretical single-scattering curves the photometric τ's displayed in Fig. 16 have been used, accounting for the decreasing trend of the curve ($I_{\rm ss}$ would be more weakly decreasing for a fixed $\tau_{\rm phot} \sim 0.45$). In the right-hand frame the scaled intensity $I/I_{\rm ss}$ is shown, normalized to unity at $B = B' = 24°$, so it is directly comparable to the Cuzzi et al. (2002) figure. Since for small elevations and small phase angles the brightness is expected to be dominated by single-scattering, this scaled intensity should be nearly constant for the case of classical low-volume-density rings. Moreover, when the non-zero volume density is taken into account (the spatially uniform models; 'ng') the scaled intensity in fact increases with $B = B'$. However, Fig. 17 also indicates that the trend reverses in the presence of gravity wakes, due to increased visibility of gaps for larger elevations. The amplitude of this inverse tilt effect, about −10% between $B = 4°$–$24°$ in the gravitating case with identical particles, is in qualitative agreement with Fig. 8 of Cuzzi et al., 2002. In the size distribution model the trend is still present although considerably weaker. According to our models, this type of contribution to the tilt effect is expected whenever the wakes are strong enough to cause significant asymmetry.

4. Discussion and summary

Photometric modeling of gravity wakes obtained in dynamical N-body simulations has been carried out in a straightforward manner by the Monte Carlo (MC) technique described in Paper I. We assumed that the layer of simulation particles is illuminated by a large number of photons, arriving either from the Sun or from Saturn, and followed the path of each photon through its successive scatterings until it was able to escape from the layer. The direct MC-method was augmented with an indirect MC method, significantly reducing the variance of the final result. The periodic boundary conditions of the dynamical simulation were taken explicitly into account, which is very important in modeling of low illumination and viewing elevations.

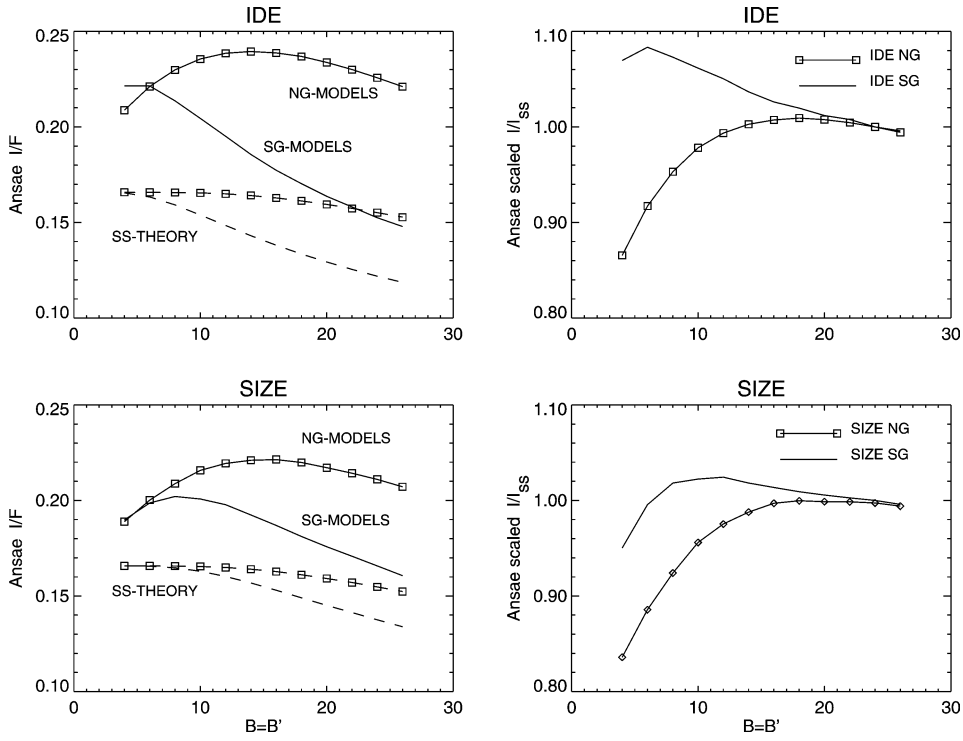

Fig. 17. The inverse tilt effect in the presence of wakes. In the left frames the ansa brightnesses are shown for photometric models utilizing 4 different dynamical simulations: standard identical particle and size distribution models ("sg-models") and corresponding models without self-gravity (marked by symbols; "ng-models"). Also shown are theoretical single-scattering contributions, calculated with the classical formula using the appropriate $\tau_{\rm path}$ for each elevation. At right the scaled $I/I_{\rm ss}$, explained in the text, is shown, with the curves normalized by values at $B = B' = 24°$. Whereas in the case of spatially uniform non-gravitating models, the scaled $I/I_{\rm ss}$ increases slightly with $B = B'$, the opposite trend occurs for the case of wakes. The figure can be compared to Fig. 8 in Cuzzi et al. (2002), showing the same type of observed reversed behavior for the portion of the A ring where the asymmetry is strongest.

In order to apply the method to modeling of the brightness asymmetry, we assume that the particle positions obtained from dynamical simulations sample the typical particle distributions at each ring longitude, in a coordinate system aligned with the local radius vector. For a given viewing geometry, each longitude of the rings has its specific illumination and viewing direction, for which the ring brightness is calculated. Since wakes are transient, time-dependent features, simulation snapshots from several time steps are employed, corresponding to the spatial averaging present in any observations covering a large number of unresolved wakes. Two different dynamical models were used in photometric modeling, one with identical particles and the other with a truncated power-law size distribution ($r_{\rm max}/r_{\rm min} = 10, q = 3$). In both cases the saturnocentric distance $a =$ 130,000 km, dynamical optical depth $\tau_{\rm dyn} = 0.5$, surface density $\Sigma = 500\ {\rm kg\,m^{-2}}$, internal density $\rho = 450\ {\rm kg\,m^{-3}}$ and the Bridges et al. (1984) velocity-dependent coefficient of restitution were assumed. The effects of various geometric factors on the obtained brightness curves were then studied.

For both dynamical models, the overall brightness vs. longitude curve was in rough agreement with the behavior of reflected and transmitted light as seen in Voyager observations. For the model of identical particles the amplitude of the asymmetry in reflected light was in fact rather close to observations, but the match was clearly worse in the case of the size distribution. This clearly indicates that the assumed dynamical parameters need refinements. An obvious parameter to reconsider is the adopted value of the dynamical optical depth, especially since the models themselves indicate that the resulting $\tau_{\rm phot} \approx 0.3$–$0.4$ of the models is in fact below the observed value ~ 0.5. Indeed, increasing $\tau_{\rm dyn}$ would increase the asymmetry amplitude also in the case of size distribution models.

Even though the longitude of the modeled brightness minimum differed by a few degrees from the observed value (245° vs. 249°, for the geometry studied in Dones et al., 1993), the models were able to provide an explanation for the asymmetric shape of the minimum, in terms of the brightness depending on both the viewing and illumination longitudes. The model brightness seems to be somewhat more sensitive to the illumination direction, in the sense that the gradient of I/F in the models is larger on the side of the minimum corresponding more closely to illumination along the wakes, in qualitative agreement with observations. This follows from the particular geometry studied, where the solar elevation is smaller than the viewing elevation. Nevertheless, for low α the modeled minimum in reflected light fell very nearly at the average of the longitudes which correspond to parallel viewing and illumination of wakes. This is not very different from what was reported in Dones et al. (1993): for the images FDS 43916.44–43917.12, with $B =$

12.6°, $B' = 8.0°$, and $\Delta\theta_s = 10.3°$, they measured a minimum at $\theta_0 = 249°$, whereas for the image FDS 43974.43 with $B = 16.5°$, $B' = 8.0°$, $\Delta\theta_s = 18.1°$ the observed minimum was shifted to $\theta_0 = 246°$, or 3° further away from the ansa. Photometric modeling with these parameters yields a minimum at 242°, similarly shifted by 3° in comparison to 245° obtained for the previous values. This modeled value for $\Delta\theta_s = 18.1°$ is also roughly consistent with the estimate of Eq. (18), which gives

$$\theta_0 = 270° - \phi_{\text{wake}} - \frac{1}{2}\Delta\theta_s - \frac{1}{2}\Delta\theta_0 \approx 270° - 21° - 9.0° - (-2.5°) \approx 242.5°. \quad (23)$$

(For this close range image $\Delta/a = 10.3$, giving $\Delta\theta_0 \approx -5°$ near the eastern ansa.) For a wider range of $\theta_s - \theta_0$ the brightness profile depends on solar longitude in a more complicated way.

In order to further illustrate how the modeled I/F vs. θ_0 curves are modified for close-range geometry, Fig. 18 shows the full 360° range plots of the models corresponding to images FDS 43916.44 and FDS 43974.43 (ignoring shadowing of the rings by the planet). As seen, the modeled I/F's are different for the two ansae, and the modeled minima are also at different distances from the ansae, even though the underlying dynamical model is symmetrical with respect to a 180° shift in ring longitude. The difference is due to the different local directions between viewing and illumination longitudes. For the eastern ansa ($\theta_0 \approx 270°$) the longitude difference

$$\phi_s - \phi_0 = -\Delta\theta_s + \Delta\theta_0 \quad (24)$$

is for this geometry significantly larger than for the western ansa, reducing the overall brightness level. The local viewing elevations and phase angles are also slightly different, but their effect is negligible.

Altogether, it seems that our modeling accounts fairly well for the shift of the brightness minimum with $\Delta\theta_s$, at least for small-α observations, when the distance-dependent geometric factors are taken into account. The slight error in the minimum longitudes themselves suggests that the effective pitch angle of wakes is a few degrees smaller than implied by our present dynamical model. Again, increasing the modeled τ_{phot} might help, even if the dynamical pitch angle would remain the same, since the larger optical depth might be expected to make the low density tails of wakes more efficient in determining the photometric behavior: ac-

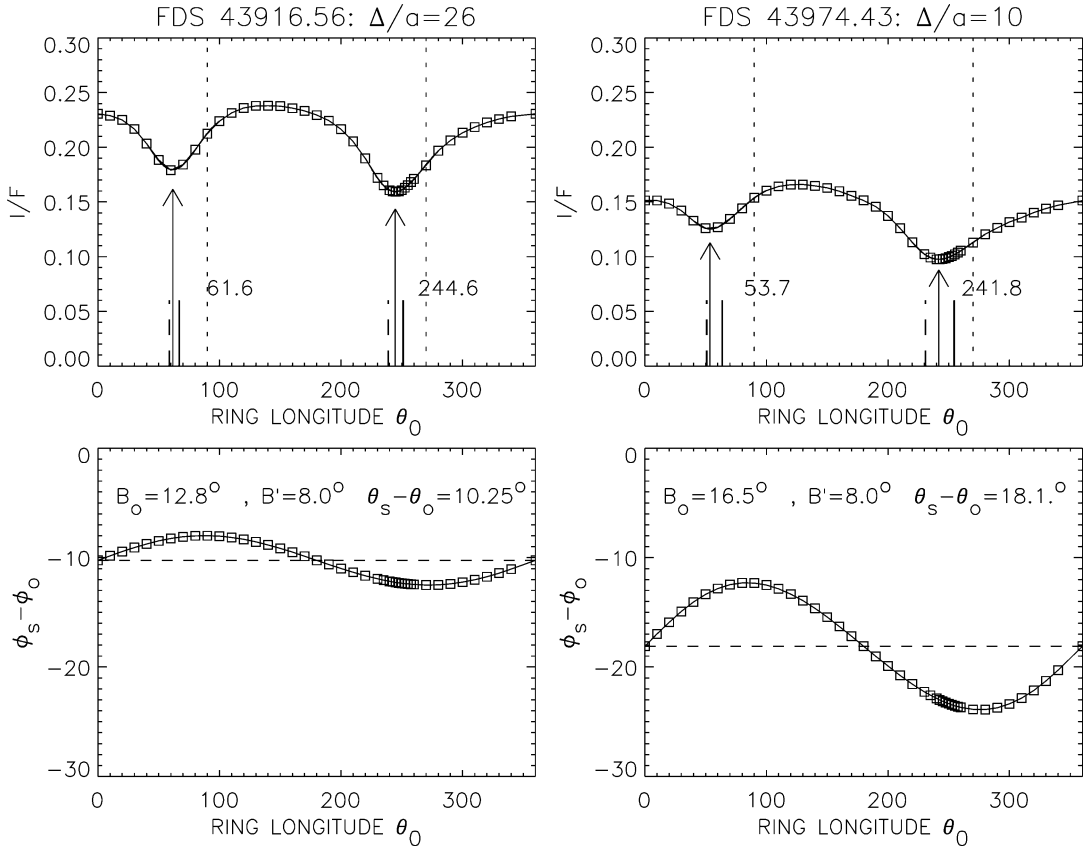

Fig. 18. Models of full 360° brightness vs longitude curves for two close-range Voyager images analyzed in Dones et al. (1993). The upper frames show the I/F curves, while the lower ones display the difference in the viewing and illumination longitudes, $\phi_s - \phi_0$. For infinite distance this would equal $-\Delta\theta_s$, shown with the dashed line (the lower left/right image corresponds to the upper left/right frame). In the upper frames the arrows indicate the minima near the two ansae, while the dashed (solid) ticks indicate the longitudes where illumination (viewing) is closest to being parallel to wakes, with an average pitch angle of 21°.

cording to the autocorrelation plot (Fig. 5) these tails have a smaller angle with respect to the tangential direction.

For transmitted light the minimum location was also quite successfully accounted for, although the only observational data analyzed is for geometries where the Saturn-shine is also large, causing some uncertainty in the extraction of the direct solar contribution. Somewhat counterintuitively, the same general longitude dependence was seen as in the reflected light. Nevertheless, when very small elevations and phase angles were modeled, the situation became reversed as compared to reflected light, as envisioned in Franklin et al. (1987).

The trend of the asymmetry amplitude with elevation angle we find matches fairly closely that found in the ground-based observations from the 1970's (Lumme and Irvine, 1976a, 1979b; Lumme et al., 1977; Thompson et al., 1981), the amplitude peaking at intermediate elevations. The models also predict a change in the width and the location of the minimum with increasing elevation (the minimum widening and moving slightly away from the ansa), but the limited accuracy of these early observations does not allow even qualitative comparisons. Basically, we suggest the asymmetry to be dominated by single scattering, but as the multiply-scattered contribution exhibits a similar and even stronger longitude variation, the asymmetry amplitude may depend on wavelength via the single-scattering albedo. This is also consistent with observations (Lumme et al., 1977), although the observed effect might be even larger than implied by the simulation models we studied. If so, this problem could arise due to the too small optical depth in our present models, which reduces the role of multiple scattering. The models also predict a reduction in the asymmetry amplitude near opposition, due to reduced intrinsic variation of singly-scattered flux. Again, this is at least qualitatively consistent with Lumme et al. (1977)'s observations. It will be very interesting to compare all these aspects of the modeled asymmetry with the recent Hubble Space Telescope observations, described in Cuzzi et al. (2002), covering a wide range of ring elevations and phase angles, with high accuracy observations in several wavelengths (French et al., in preparation).

The strong dependence of the modeled optical depth on the viewing direction with respect to wakes is a factor that is likely to be present wherever the presence of wakes may be suspected based on azimuthal brightness variations. Clearly, in the presence of wakes the normal optical depth deduced from occultation measurements will depend sensitively on both the elevation and ring longitude of the scan if Eq. (21) for $\tau_{\rm phot}$ is used. In particular, this dependence should be taken into account when interpreting occultation optical depth profiles of the A ring, to be obtained during Cassini's orbital tour.

An important new result is the natural explanation the wakes offer for the inverse tilt effect (Cuzzi et al., 2002) seen in those regions of the A ring where the asymmetry is strongest. According to our models (see Fig. 17) this follows from the reduced brightness of the ring as more and more of the rarefied inter-wake regions become visible with increasing elevation. Altogether, this observational phenomenon may be considered as additional very strong evidence of wakes, besides the asymmetry itself.

Even if the wakes are likely to exist in A-ring, it is uncertain whether Cassini will be able to resolve them directly. According to Eq. (4), the expected radial scale of wakes is at most about 100 meters, still below even the best resolution of Cassini images. Nevertheless, Fourier analysis and/or wavelet analysis of the UVIS high-resolution occultation profiles should be able to show if excess signal is present in these wavelengths. If resolved, the radial scale of wake structure will give accurate constraints for the local surface density of rings, complementing those derived from satellite excited density waves. Also, the mere confirmation of wakes, resolved or not, would already give an estimate of the local velocity dispersion in terms of Toomre parameter being close to unity.

5. Conclusions

According to our models:

- Gravitational wakes account in detail for the observed brightness-longitude dependence seen in Voyager observations of the A ring, both for the reflected and transmitted radiation. The minimum brightness corresponds to viewing roughly along the wakes, minimizing the scattering area.
- Basically similar behavior is predicted for both reflected and transmitted radiation, except in the case B and B' close to zero, when the minimum and maximum longitudes are reversed in transmitted light (i.e., the brightness maximum corresponds to viewing and illumination along wakes).
- The variations of asymmetry amplitude with ring opening angle, and its peak for intermediate elevations $\sim 12^\circ$ is well accounted for. Also, the suggested trend of amplitude increasing with increased wavelength, as well as the reduction of amplitude at opposition, seem to be in qualitative agreement with observations.
- Wakes provide a natural explanation for the inverse tilt-effect of the mid A ring, the brightness being reduced as the rarefied region between wakes become better visible at larger elevations.
- The presence of wakes needs to be taken into account in the interpretation of Cassini stellar occultation profiles, as well as Voyager and Earth-based stellar occultations.

On the quantitative level several problems remain in explaining the observed asymmetry. In particular, although our models with identical particles yielded a roughly correct asymmetry amplitude, the amplitude obtained in the, presumably more realistic, size distribution model was smaller than observed. Also, the photometric optical depth of the

models was somewhat smaller than the actual A-ring values. This clearly indicates that the dynamical parameters adopted here are not optimal. Our future study will address in a systematic manner the dependence of azimuthal asymmetry on various dynamical parameters, like the internal density and elasticity of particles, and the underlaying dynamical optical depth. An important constrain for this survey, as well as for any quantitative model of Saturn ring's structure, is provided by the strong peaking of the observed asymmetry amplitude in the mid A-ring.

Acknowledgments

This work was supported by the Academy of Finland, the Väisälä Foundation, and by the NASA Planetary Geology and Geophysics Program. We thank Luke Dones and David Dunn for their very detailed and helpful reviews.

References

Barkstrom, B.J., 1973. A comparison of the Minneart reflectance law and the reflectance from a nonconservative isotropic scattering atmosphere. J. Geophys. Res. 78, 6370–6372.

Brahic, A., 1977. Systems of colliding bodies in a gravitational field. Astron. Astrophys. 54, 895–907.

Bridges, F.G., Hatzes, A., Lin, D.N.C., 1984. Structure, stability and evolution of Saturn's rings. Nature 309, 333–335.

Camichel, H., 1958. Mesures photométriques de Saturne et de son anneau. Ann. Astrophys. 21, 231–242.

Colombo, G., Goldreich, P., Harris, A.W., 1976. Spiral structure as an explanation for the asymmetric brightness of Saturn's A ring. Nature 264, 344–345.

Cuzzi, J.N., French, R.G., Dones, L., 2002. HST multicolor (255–1042 nm) photometry of Saturn's main rings. I. Radial profiles, phase and opening angle variations, and regional spectra. Icarus 158, 199–223.

Daisaka, H., Ida, S., 1999. Spatial structure and coherent motion in dense planetary rings induced by self-gravitational instability. Earth Planets Space 51, 1195–1213.

Dones, L., Porco, C.C., 1989. Spiral density wakes in Saturn's A ring? Bull. Am. Astron. Soc. 21, 929. Abstract.

Dones, L., Cuzzi, J.N., Showalter, M.R., 1993. Voyager photometry of Saturn's A ring. Icarus 105, 184–215.

Dunn, D.E., Molnar, L.A., Fix, J.D., 2002. More microwave observations of Saturn: modeling the ring with a Monte Carlo radiative transfer code. Icarus 160, 132–160.

Dunn, D.E., Molnar, L.A., Niehof, J.T., de Pater, I., Lissauer, J.L., 2004. Microwave observations of Saturn's rings: anisotropy in directly transmitted light. Icarus. In press.

Esposito, L.W., 1979. Extension to the classical calculation of the effect of mutual shadowing in diffuse reflection. Icarus 39, 69–80.

Ferrin, I., 1975. On the structure of Saturn's rings and the "real" rotational period for the planet. Astrophys. Space Sci. 33, 453–457.

Franklin, F.A., Colombo, G., 1978. On the azimuthal brightness variations of Saturn's rings. Icarus 33, 279–287.

Franklin, F.A., Cook, A.F., Barrey, R.T.F., Roff, C.A., Hunt, G.E., de Rueda, H.B., 1987. Voyager observations of the azimuthal brightness variations in Saturn's rings. Icarus 69, 280–296.

French, R.G., Nicholson, P.D., 2000. Saturn's rings II. Particle sizes inferred from stellar occultation data. Icarus 145, 502–523.

French, R.G., Dones, L., Salo, H., 2000. HST observations of the azimuthal brightness asymmetry in Saturn's rings. Bull. Am. Astron. Soc. 32, 864. Abstract.

Fridman, A.M., Gorkavyi, N.N., 1999. Physics of Planetary Rings. Springer-Verlag, New York.

Goldreich, P., Tremaine, S.D., 1978. The velocity dispersion in Saturn's rings. Icarus 34, 227–239.

Gorkavyi, N.N., Taidakova, T.A., 1989. Nature of the azimuthal asymmetry of the brightness of Saturn's rings. Sov. Astron. Lett. 15, 234–237.

Hämeen-Anttila, K.A., 1978. An improved and generalized theory for the collisional evolution of Keplerian systems. Astrophys. Space Sci. 58, 477–519.

Hämeen-Anttila, K.A., Itävuo, H., 1976. East–west asymmetry of Saturn's rings. Astrophys. Space Sci. 41, 57–61.

Hämeen-Anttila, K.A., Vaaraniemi, P., 1975. A theoretical photometric function of Saturn's rings. Icarus 25, 470–478.

Julian, W.H., Toomre, A., 1966. Non-axisymmetric responses of differentially rotating disks of stars. Astrophys. J. 146, 810–830.

Karjalainen, R., Salo, H., 2004. Gravitational accretion of particles in Saturn's rings. Icarus. Submitted for publication.

Karttunen, H., 1983. The wake model for azimuthal brightness variations in Saturn's A-ring. Moon Planets 29, 117–120.

Lumme, K., Irvine, W.M., 1976a. Azimuthal brightness variations of Saturn's rings. Astrophys. J. 204, L55–L57.

Lumme, K., Irvine, W.M., 1976b. Photometry of Saturn's rings. Astron. J. 81, 865–893.

Lumme, K., Irvine, W.M., 1979a. A model for the azimuthal brightness variations in Saturn's rings. Nature 282, 695–696.

Lumme, K., Irvine, W.M., 1979b. Azimuthal brightness variations of Saturn's rings. III. Observations at tilt angle B approximately equal to 11.5 deg. Astrophys. J. 229, L109–L111.

Lumme, K., Esposito, L.W., Irvine, W.M., Baum, W.A., 1977. Azimuthal brightness variations of Saturn's rings. II. Observations at an intermediate tilt angle. Astrophys. J. 216, L123–L126.

Lumme, K., Irvine, W.M., Esposito, L.W., 1983. Theoretical interpretation of the ground-based photometry of Saturn's B ring. Icarus 53, 174–184.

Marouf, E.A., Tyler, G.L., Zebker, H.A., Simpson, R.A., Eshleman, V.R., 1983. Particle size distributions in Saturn's rings from Voyager 1 radio occultation. Icarus 54, 189–211.

Ohtsuki, K., 1993. Capture probability of colliding planetesimals—dynamical constraints on accretion of planets, satellites, and ring particles. Icarus 106, 228–246.

Ohtsuki, K., Emori, H., 2000. Local N-body simulations for the distribution and evolution of particle velocities in planetary rings. Astron. J. 119, 403–416.

Peltoniemi, J.I., Lumme, K., 1992. Light scattering by closely packed particulate media. J. Opt. Soc. Am. A 9, 1320–1326.

Piironen, J.O., Lukkari, J., 1980. The east–west asymmetry of Saturn's rings—a possible indicator of meteoroids. Moon Planets 23, 373–377.

Porco, C.C., Throop, H.B., Richardson, D.C., 2001. Light scattering in Saturn's rings: basic disk properties and the A ring azimuthal asymmetry. Bull. Am. Astron. Soc. 33, 1091–1092. Abstract.

Reitsema, H.J., Beebe, R.F., Smith, B.A., 1976. Azimuthal brightness variations in Saturn's rings. Astron. J. 81, 209–215.

Salo, H., 1992. Gravitational wakes in Saturn's rings. Nature 359, 619–621.

Salo, H., 1995. Simulations of dense planetary rings. III. Self-gravitating identical particles. Icarus 117, 287–312.

Salo, H., Karjalainen, R., 1999. Dynamical and photometric modeling of azimuthal brightness asymmetry in Saturn's rings. Bull. Am. Astron. Soc. 31, 1160. Abstract.

Salo, H., Karjalainen, R., 2003. Photometric modeling of Saturn's rings: I. Monte Carlo method and the effect of nonzero volume filling factor. Icarus 164, 428–460. Paper I.

Salo, H., Karjalainen, R., French, R.G., 2000. Modeling the azimuthal brightness asymmetry in Saturn's rings. Bull. Am. Astron. Soc. 32, 863. Abstract.

Thompson, W.T., 1982. The swarm model for the azimuthal brightness variations in Saturn's ring A. PhD thesis. Univ. of Massachusetts, Amherst.

Thompson, W.T., Lumme, K., Irvine, W.M., Baum, W.A., Esposito, L.W., 1981. Saturn's rings—azimuthal variations, phase curves, and radial profiles in four colors. Icarus 46, 187–200.

Toomre, A., 1964. On the gravitational stability of a disk of stars. Astrophys. J. 139, 1217–1238.

Toomre, A., Kalnajs, A.J., 1991. Spiral chaos in an orbital patch. In: Sundelius, B. (Ed.), Dynamics of Disc Galaxies. Almquist-Wiksell, pp. 341–358.

van der Tak, F.E., de Pater, I., Silva, A., Millan, R., 1999. Time variability in the radio brightness distribution of Saturn. Icarus 142, 125–147.

Wisdom, J., Tremaine, S., 1988. Local simulations of planetary rings. Astron. J. 95, 925–940.